



1                   Safer This Way: Identifying Flooded Roads for  
2                   Facilitating Mobility During Floods

3     Pranavesh Panakkal<sup>a</sup>, Allison M. Wyderka<sup>a</sup>, Jamie E. Padgett<sup>a,b</sup>, Philip B.  
4                   Bedient<sup>a</sup>

5                   <sup>a</sup>*Department of Civil and Environmental Engineering, Rice University, 6100 Main  
6                   Street, Houston, 77005, Texas, USA*

7                   <sup>b</sup>*Corresponding author, Email address: jamie.padgett@rice.edu*

---

8                   **Abstract**

9     Severe storms and associated flooding pose a significant risk to urban mobil-  
10   ity. Consequently, 40 to 63% of flood-related deaths are linked to roadway-  
11   related incidents in developed countries. The dynamic nature of flooding and  
12   the lack of real-time information make it challenging to sense flooding and  
13   its impact on roadways. Hence, existing state-of-the-art methods fall short  
14   of providing a robust, reliable, and affordable tool to facilitate situational  
15   awareness during storms. Such a tool is indispensable to aid emergency re-  
16   sponse, especially considering the potential increase in risk to flood exposure  
17   due to climate change and other factors. This study addresses this need by  
18   providing an open-source framework that couples real-time rainfall data, a  
19   physics-based flood model, and network and spatial analyses to sense real-  
20   time flood impact on the road transportation system. Case studies using  
21   three recent storms in Houston, Texas demonstrate the framework's ability  
22   to provide vehicle-class specific roadway conditions for even minor roads and  
23   residential streets—a problem existing approaches struggle with. Aside from  
24   road-link conditions, the framework can also estimate network-level flood im-

25 pacts, such as identifying regions without access to critical facilities like hos-  
26 pitals, giving decision-makers a more holistic view of network performance.  
27 Further, the framework is interoperable with existing situational awareness  
28 tools and could augment their ability to sense road conditions during flood-  
29 ing. Finally, the proposed framework can equip flood-prone communities  
30 and emergency responders with reliable and accessible situational awareness  
31 content using open-source tools and data to promote safer mobility during  
32 flooding—a key goal of intelligent transportation systems.

33 *Keywords:* Floods, radar, urban mobility, situational awareness,  
34 emergency response, alert systems.

---

35 **1. Introduction**

36 Facilitating safe mobility by providing timely and reliable information  
37 on roadway status is one of the primary goals of an intelligent transporta-  
38 tion system (ITS) (Guerrero-Ibez et al., 2018; Sumalee and Ho, 2018). Cur-  
39 rent ITS frameworks and research (Zhu et al., 2019; Sumalee and Ho, 2018;  
40 Guerrero-Ibez et al., 2018) predominantly focus on enhancing safety dur-  
41 ing normal operating conditions and provide insufficient information dur-  
42 ing adverse weather events such as floods (Dey et al., 2015). This lim-  
43 ited focus is concerning because mobility-related incidents are the leading  
44 cause (40 to 63%) of flood casualties in many developed countries (Han and  
45 Sharif, 2021). Many factors such as risk-taking behavior (Jonkman, 2007;  
46 Maples and Tiefenbacher, 2009) and insufficient information on road condi-  
47 tions (Maples and Tiefenbacher, 2009) contribute to the high flood fatalities  
48 on roads. Further, climate change and land-use change are expected to in-

49 increase the frequency and intensity of extreme flood events (Winsemius et al.,  
50 2016; Field et al., 2012). Increased flood hazard, combined with increased  
51 flood exposure (Jongman et al., 2012), could exacerbate flood-related road  
52 fatalities. These factors emphasize the need for reliable and accessible sit-  
53 uational awareness systems for ensuring safe mobility during future flood  
54 events. Situational awareness is defined here as the real-time knowledge of  
55 the road network condition at the link and network levels.

56 Several studies have proposed frameworks to address the need for reliable  
57 situational awareness tools. These frameworks can be broadly categorized  
58 into two: frameworks that directly observe flooded roads using physical, so-  
59 cial, or remote sensors, and frameworks that indirectly infer road conditions  
60 by coupling rainfall observations with mathematical flood routing models.  
61 While existing frameworks have their advantages and perform sufficiently  
62 for their use cases, they fall short of providing a comprehensive, equitable,  
63 stand-alone situational awareness tool to sense road and network level flood  
64 impacts. To elaborate, while a network of physical sensors such as auto-  
65 mobile radar (Viikari et al., 2009), cameras (Lo et al., 2015), and water  
66 depth gages (Harris County Flood Control District, 2022a) can sense the  
67 road surface condition as well as flood inundation for an urban region, it  
68 is prohibitively expensive to deploy them at optimal spatial density due to  
69 the cost associated with deployment, operation, maintenance, and security  
70 (Jiang et al., 2018). Such expensive systems are especially unattainable for  
71 socioeconomically disadvantaged communities who are also often dispropor-  
72 tionately affected by flooding and potential climate change impacts (Levy  
73 and Patz, 2015).

In urbanized regions with active users, social sensors such as crowdsourcing (e.g., Waze (Google LLC, 2022a)) (Prahraj et al., 2021) and social media analytics (e.g., Twitter (Twitter, Inc., 2022)) (Fan et al., 2020b) can provide superior spatial coverage than physical sensors. At the same time, they might introduce bias (Fan et al., 2020a), noise (He et al., 2017), and significant time lags between the occurrence of an event and its detection (De Longueville et al., 2009). These limitations, together with potential for misinformation and lack of quantitative flood depth estimates, render social sensors lacking as the sole source for situational awareness, especially considering that a majority of flood fatalities are caused by flash floods (Han and Sharif, 2021). Similarly, remote sensors such as satellite images (Ahmad et al., 2019) and unmanned aerial vehicles (Perks et al., 2016) might not be suitable for real-time applications due to limited availability during inclement weather, significant time lag between revisit times of satellites, and obstacles such as clouds and vegetation (Jiang et al., 2018). Synthetic Aperture Radar can potentially improve flood monitoring by overcoming some drawbacks of conventional satellite remote sensing (Carreño Conde and De Mata Muñoz, 2019; Landuyt et al., 2018). However, the time lag between revisit times still limits their application in real-time emergency response applications. Further, recent advances in deep learning and image processing (Geetha et al., 2017; Jiang et al., 2018; Chaudhary et al., 2019) offer promising methods for estimating flood depth from low-resolution images. Additional model development and testing under operational conditions such as low light, fog, and glare are required to further enhance the generalizability of image processing models. Finally, though authoritative sources such as traffic information and

99 warning systems (Texas Department of Transportation, 2022) provide road  
100 closure alerts, the data availability is usually limited to major highways.

101 While direct flood observations are reliable, they are not always available;  
102 an alternative is to leverage real-time rainfall observations and physics-based  
103 flood models to infer road conditions. Though past studies have demon-  
104 strated the capability of physics-based models to estimate flood impacts (Gori  
105 et al., 2020; Coles et al., 2017; Yin et al., 2017; Green et al., 2017; Pyatková  
106 et al., 2019; Hackl et al., 2018; Evans et al., 2020; Pregnolato et al., 2017),  
107 they primarily focused on offline applications such as vulnerability and risk  
108 assessment. Some recent studies (Panakkal et al., 2019; Mioc et al., 2015;  
109 Ming et al., 2020; Naulin et al., 2013; Versini et al., 2010; Morsy et al., 2018;  
110 Johnson et al., 2018) show that combining real-time rainfall data with flood  
111 models is a viable alternative to frameworks relying solely on direct flood  
112 observations; notably, they excel in two critical areas: availability and af-  
113 fordability. These studies have shown that state-of-the-art flood models can  
114 reliably estimate the flood conditions over a large area and can be built us-  
115 ing open-source data and technologies easily accessible to most flood-prone  
116 communities (Morsy et al., 2018; Ming et al., 2020; Mudashiru et al., 2021;  
117 Brunner, 2021; National Oceanic and Atmospheric Administration, 2016).

118 Current frameworks that leverage flood models fail to provide a com-  
119 prehensive tool for mobility-centric situational awareness. Many existing  
120 physics-based frameworks limit flood prediction to specific watchpoints in the  
121 watershed (such as bridges and roads adjacent to streams) or capture only  
122 riverine floods. For example, the National Water Model (National Oceanic  
123 and Atmospheric Administration, 2016; Johnson et al., 2019) used in John-

124 son et al. (2018) provides high-quality flow predictions for streams across the  
125 U.S. but does not provide pluvial flooding predictions or water velocity data,  
126 which are both critical for inferring network-level impacts of flooding and  
127 vehicle safety. Both pluvial and fluvial floods represent a considerable risk  
128 to roadway mobility in urban areas. Consequently, models capturing flood  
129 impacts on transportation throughout the watershed are essential. Further,  
130 existing frameworks also lack a scalable method to consider roadway topog-  
131 raphy (elevated vs. at-grade roads) when determining flooded roadways and  
132 thus could overestimate flood impacts.

133 Additionally, state-of-the-art physics-based and observation-based frame-  
134 works showed limited to no consideration of vehicle characteristics and network-  
135 level impacts of flooding (Johnson et al., 2018; Ahmad et al., 2019; Ming  
136 et al., 2020; Naulin et al., 2013; Morsy et al., 2018; Texas Department of  
137 Transportation, 2022; Google LLC, 2022a). Observing water does not imply  
138 the road is impassable to all vehicles (e.g., passenger cars vs. high-water vehi-  
139 cles); a road is impassable for a vehicle if flood conditions (inundation depth  
140 and flow velocity) pose a safety risk. By neglecting the vehicle characteristics  
141 in identifying flooded roads, existing methods could misclassify roads and en-  
142 danger emergency responders. Similarly, while identifying flooded road links  
143 is necessary, it alone is insufficient for emergency response decision-making.  
144 Providing a holistic view of flood impacts on access to communities and crit-  
145 ical facilities, such as hospitals, is vital for timely response and evacuation  
146 during flooding.

147 In conclusion, there is a need to address gaps in the current suite of  
148 situational awareness tools to enhance roadway safety under present and

149 future flooding. Such a system, in addition to being reliable, affordable, and  
150 available with a limited time lag, should also a) be available for a majority  
151 of roads; b) be capable of identifying link- and network-level impacts of  
152 flooding; and c) consider vehicle characteristics and roadway topography to  
153 provide vehicle-specific road condition. This study addresses these needs via  
154 a new real-time situational awareness system called open-source situational  
155 awareness framework for mobility (OpenSafe Mobility).

156 OpenSafe Mobility leverages a physics-based flood model instead of sen-  
157 sors to infer flood conditions. It combines gage-adjusted radar rainfall, a  
158 rainfall-runoff flood model, and network and spatial analyses to infer flood  
159 conditions of roads and quantify the network-level flood impacts on mobil-  
160 ity. Furthermore, while OpenSafe Mobility can function independently, it is  
161 designed to be interoperable with existing ITS frameworks via the Represen-  
162 tational State Transfer (REST) Application Programming Interface (API)  
163 access.

## 164 2. The Proposed Architecture

165 This section describes the OpenSafe Mobility architecture (Fig. 1). First,  
166 real-time radar rainfall data are collected and processed to identify flood-  
167 inducing rainfall (Fig. 1a). For events that could cause flooding, a select  
168 duration of the radar rainfall data (referred to as the maximum considered  
169 duration or  $d_{max}$ ) preceding the last available radar data is collected and pro-  
170 cessed (Fig. 1b). The considered rainfall duration  $d_{max}$  should be sufficient  
171 to accurately model flood impacts in the study region. Next, a physics-based  
172 rainfall-runoff flood model (Fig. 1b) uses the processed radar rainfall data

173 to infer the current flood conditions. Flood hazards at road links and vehicle  
174 characteristics are then used to identify flooded roads for select vehicle classes  
175 (Fig. 1c). Next, OpenSafe Mobility uses the road condition data to estimate  
176 network-level impacts of road closures on roadway access to critical facilities  
177 such as fire stations and hospitals (Fig. 1d). The OpenSafe Mobility results  
178 can help find safe routes between origin-destination pairs and identify regions  
179 without access to critical facilities such as hospitals. Finally, the results are  
180 communicated to stakeholders through a web interface and REST API (Fig.  
181 1e).

182 *2.1. Radar Rainfall Data*

183 For accurate flood modeling, reliable and robust real-time rainfall data  
184 that captures the temporal and spatial variability of rainfall is essential.  
185 Three common sources of rainfall data are rain gages, radar rainfall, and  
186 gage-adjusted radar rainfall (GARR). GARR fuses observations from rain  
187 gages (which on their own suffer from spatial availability) and radar data  
188 (which on its own suffers from accuracy) to provide a more complete spa-  
189 tial and temporal distribution of rainfall with higher reliability (Fang et al.,  
190 2011; Vieux & Associates, Inc., 2022). Consequently, OpenSafe Mobility uses  
191 GARR for real-time rainfall data. Depending on the cost and availability of  
192 the sources in the study region, OpenSafe Mobility can also be tailored to  
193 use any of the three sources.

194 During operation, OpenSafe Mobility acquires spatial rainfall data at  
195 regular intervals. Since all events do not produce flooding, tracking rainfall  
196 and initiating further analysis only for flood-inducing events (as indicated  
197 by exceeding a threshold) can promote optimal use of computing resources.

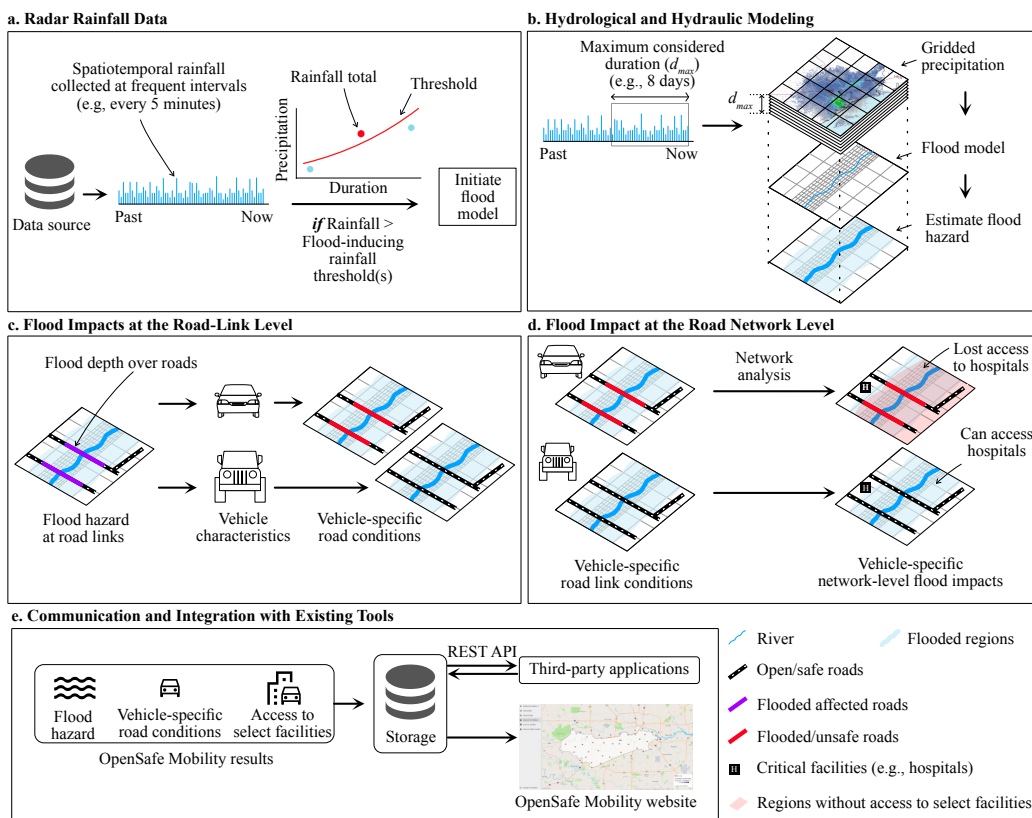


Figure 1: Overview of OpenSafe Mobility. Image source: National Weather Service (2022); Google LLC (2022b)

198 The threshold flood-inducing rainfall depends on the characteristics of the  
199 study region and can be obtained from either historical data or hydrological  
200 studies. In the absence of detailed hydrological studies, such as Dao et al.  
201 (2020), point precipitation frequency estimates and historical flooding in the  
202 study region can be used to define flood inducing thresholds. For example,  
203 in many parts of Houston, the stormwater network is designed to carry a  
204 2-year storm (Haddock and Kanwar, 2021) and any rainfall exceeding the  
205 threshold (say 5-year event) could overwhelm the drainage system and result  
206 in flooding. Fig. 2 illustrates an example scenario. Here, rainfall in a Brays  
207 Bayou subwatershed region is plotted in five-minute intervals (Fig. 2a) and  
208 compared against the 5-year recurrence interval for the region from NOAA  
209 Atlas-14 (Perica et al., 2018) for each time step (Fig. 2b). The observed  
210 rainfall for the subwatershed exceeded the NOAA Atlas-14 5-year thresholds  
211 on Day 26 at 19:45 for the first time during the event. Similarly, OpenSafe  
212 Mobility monitors the entire study region and initiates the model run if the  
213 threshold is exceeded at any point within the study area or at the watershed  
214 level. Once activated, OpenSafe Mobility will continue to run the model until  
215 all roads are passable.

216 Once the flood-inducing rainfall threshold is exceeded, a select duration  
217 of the rainfall (referred to as maximum considered duration  $d_{max}$ ) before the  
218 last available time step is used to run the flood model. The duration of rain-  
219 fall considered ( $d_{max}$ ) should be sufficient to estimate the flood conditions  
220 reliably. Specifically,  $d_{max}$  should be more than the time of concentration of  
221 the study region and should be sufficient to accurately capture soil moisture  
222 conditions in the watersheds and base flow in channels. Practically,  $d_{max}$  can

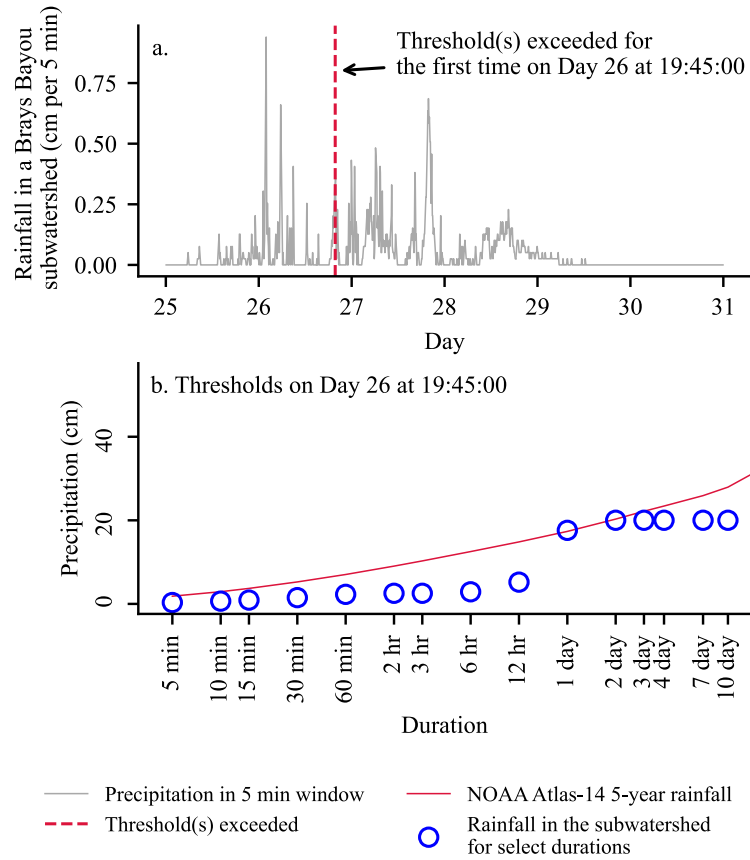


Figure 2: Example criteria for identifying flood-inducing rainfall. Here NOAA Atlas-14 5-year (20% annual probability of exceedance) recurrence interval rainfall thresholds (red line in part b) are used to initiate OpenSafe Mobility model run. The red dotted line (part a) marks the first-time step for which rainfall amounts exceeded any thresholds (red line in part b) in a select subwatershed. The rainfall totals corresponding to this time are compared against different thresholds in the bottom image (part b). OpenSafe Mobility monitors rainfall in every part of the watershed and initiates the model run if the threshold is exceeded in any location within the study area. Data sources: NOAA Atlas-14 Perica et al. (2018) and Vieux & Associates, Inc.

223 be identified by varying duration of rainfall considered for select historical  
224 storms and checking model accuracy using historical data at select watch-  
225 points in the study area. Maximum event duration  $d_{max}$  selected should  
226 also consider acceptable time lag for real-time situational awareness applica-  
227 tion. The acceptable time lag depends on stakeholder needs. For emergency  
228 response applications, a limited time lag (e.g.,  $\leq 30$  min) is preferred to en-  
229 sure the pertinency of the model predictions. The time lag consists of the  
230 time required to acquire rainfall data, process the radar, run the OpenSafe  
231 Mobility model, and publish the results. Out of these steps, the time to  
232 acquire the rainfall data and run the OpenSafe Mobility model is typically  
233 time-consuming. The time required to acquire rainfall data depends on the  
234 data source and is beyond the control of OpenSafe Mobility. The model  
235 runtime depends on the duration of rainfall, resolution of the model, study  
236 area size, and the computing resources available. Once  $d_{max}$  and acceptable  
237 time lag are identified, factors such as computing resources available and the  
238 resolution of the flood and network models are optimized to maximize model  
239 accuracy and reduce lag time. Considering an event duration less than  $d_{max}$   
240 might be necessary for larger study areas to provide approximately correct  
241 results within an acceptable time lag. For applications with longer model  
242 run time, deploying multiple machines that can asynchronously process the  
243 radar data can significantly improve data availability. Further, it would be  
244 ideal if these machines were not co-located as flood events could result in  
245 large-scale network and power outages.

246 *2.2. Hydrological and Hydraulic Modeling*

247 During flood analysis, hydrological and hydraulic analyses are performed  
248 using the input rainfall data and a calibrated 2D unsteady flow model. While  
249 several capable tools exist for 2D unsteady flow modeling (Mudashiru et al.,  
250 2021), this study uses Hydrologic Engineering Center-River Analysis System  
251 (HEC-RAS) software (version 6.0) (Brunner, 2021) from the United States  
252 Army Corps of Engineers (USACE) for flood modeling. The widespread  
253 adoption of HEC-RAS among industry (Dysarz, 2018), government agencies  
254 (Harris County Flood Control District, 2022b), and academia (Gori et al.,  
255 2020; Mudashiru et al., 2021) is especially appealing as it could facilitate  
256 easy adoption and transferability of OpenSafe Mobility. OpenSafe Mobility  
257 will leverage HEC-RAS to model both local street level (pluvial) flooding  
258 and riverine (fluvial) flooding using gridded rainfall data. Please refer to the  
259 HEC-RAS flood manual (Brunner, 2021) for more details on HEC-RAS.

260 While the version of OpenSafe Mobility presented here uses HEC-RAS,  
261 any tool that meets the following criteria can be used for real-time rainfall-  
262 runoff analysis: a) the model should efficiently perform 2D unsteady flow  
263 analysis using real-time rainfall data, accurately capturing pluvial and flu-  
264 vial flooding; b) the model should generate water surface elevation and flow  
265 velocity data at a suitable resolution to discern road conditions; and c) the  
266 model should provide automated workflows (via code or APIs) to initiate  
267 model run and extract results. Several such tools are available in the litera-  
268 ture, and Mudashiru et al. (2021) present a brief overview of flood mapping  
269 methods and tools.

270 To ensure model accuracy, the model is calibrated using select historical

271 rainfall events in the study regions and tested on unseen storms to ensure  
272 generalizability. During calibration, model parameters are iteratively modi-  
273 fied until model outputs converge to the observed stream gage readings.

274 *2.3. Using Flood Hazard Data to Estimate Vehicle-Specific Road-Link Con-*  
275 *ditions*

276 The flood model uses the gridded rainfall data to perform hydrological  
277 (rainfall-runoff simulation) and hydraulic (flow routing) simulations to infer  
278 the current flood conditions. Example variables that can quantify the flood  
279 conditions include water depth over the terrain, water surface elevation, and  
280 flow velocity. While many studies use water depth estimates to identify  
281 flooded roads, this method could introduce errors, particularly for elevated  
282 roads and bridges. The water depth map from a flood model represents the  
283 water over the bare earth surface without infrastructure elements like elevated  
284 roads and bridges. This study subtracts the elevation of roads, derived from  
285 Light Detection and Ranging (LiDAR) point clouds data, from water surface  
286 elevation data from the flood model to estimate flood depths over roads ( $d^r$ ).  
287 Fig. 3 shows an example of LiDAR point cloud data obtained from an aerial  
288 survey (Houston-Galveston Area Council, 2022) and Fig. 4 illustrates the  
289 difference between DEM used for flood analysis and a digital surface model  
290 (DSM) developed from LiDAR data that preserves roadway elevation.

291 OpenSafe Mobility provides three strategies to estimate road link status:  
292 depth-centric, probabilistic depth-centric, and stability-centric approaches.  
293 These strategies are intended to address the variability in stakeholder needs,  
294 data availability, and computing resources.

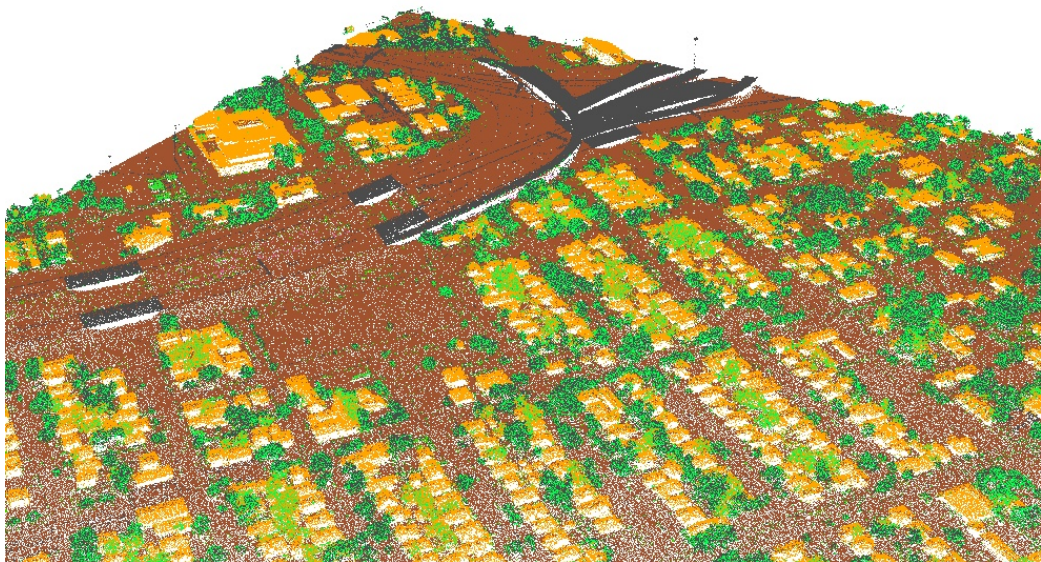


Figure 3: An example LiDAR point cloud data. Here, each point represents the elevation of that point relative to a datum. The points are color coded to categorize the point; green points indicate vegetation, yellow indicates buildings, brown indicates bare earth, and black indicates road infrastructure. Image created using LAStools (Rapidlasso GmbH, 2012). Data source: Houston-Galveston Area Council (2022).

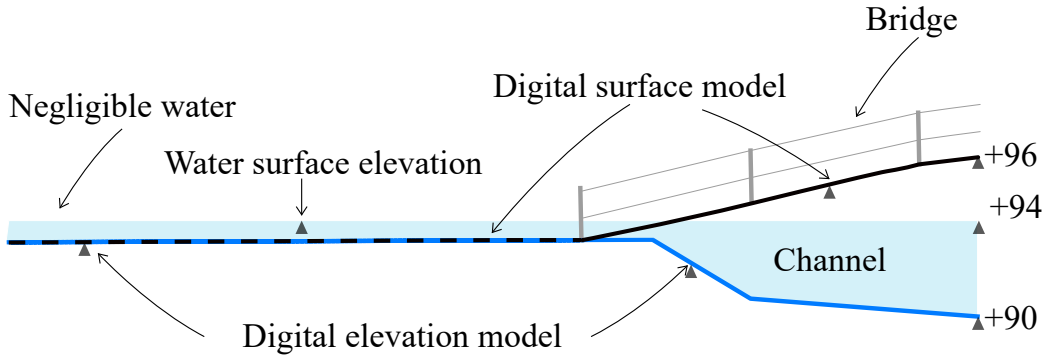


Figure 4: Comparison between a hydrologically conditioned digital elevation model (DEM) and digital surface model (DSM). Infrastructure facilities such as bridges are removed during the creation of DEM. Hence, using DEM for estimating road condition could lead to error. Alternatively, subtracting DSM from water surface elevation can reliably infer roadway condition.

*295 2.3.1. Depth-Centric Approach to Estimate Road Link Status*

*296 In the depth-centric approach (Fig. 5a-d; Eq.1), safe wading height ( $w_h$ )*  
*297 of vehicles (Contreras-Jara et al., 2018) are compared against the water depth*  
*298 over roads ( $d^r$ ) to estimate vehicle-specific roadway status ( $R^d$ ). A road is*  
*299 not traversable if the safe vehicle wading height is less than the sum of*  
*300 water depth over the road and a water depth buffer ( $\delta_d$ ). The water depth*  
*301 buffer is optional, and it provides a margin to compensate for any depth*  
*302 underestimation from the flood model or an additional margin to assure*  
*303 vehicle safety.*

$$R^d(d^r, \delta_d, w_h) = \begin{cases} \text{open}, & \text{if } w_h \geq d^r + \delta_d \\ \text{closed}, & \text{otherwise} \end{cases} \quad (1)$$

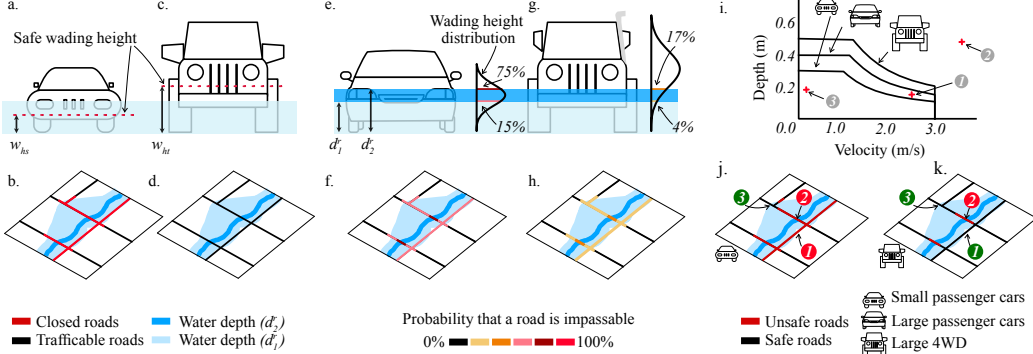


Figure 5: Depth-centric (parts a-d), probabilistic depth-centric (parts e-h), and stability-centric (parts i-k) strategies for identifying impassable roads. In the depth-centric strategy, impassable roads are identified by comparing the wading height of the vehicle with the water depth. In the probabilistic depth-centric approach, the wading height distribution of a vehicle class is used to estimate the probability of road link flooding. In the stability-centric approach, stability criteria are used to identify unsafe roads.

### 304 2.3.2. Probabilistic Depth-Centric Approach to Estimate Road Link Status

305 In the probabilistic depth-centric approach (Fig. 5e-h; Eq. 2), depth over  
 306 roads ( $d^r$ ) and wading height distribution ( $W_h$ ) (Contreras-Jara et al., 2018)  
 307 of different vehicle classes (e.g., SUVs, passenger cars) are used to estimate  
 308 the probability of a road link being impassable. Here, the probability of a  
 309 road link being impassable for a vehicle class ( $P^d$ ) is defined as the percentage  
 310 of vehicles with wading heights lesser than the water depth over the road link  
 311 plus an optional buffer ( $\delta_d$ ) (i.e,  $d^r + \delta_d$ ).

$$P^d(d^r, \delta_d, W_h) = \int_{-\infty}^{d^r + \delta_d} W_h(x) dx \quad (2)$$

312    2.3.3. Stability-Centric Approach to Estimate Road Link Status

313    The buoyancy and drag forces exerted by flood waters may cause vehi-  
 314    cles to float, slide, or overturn. Ignoring flow velocity and focusing solely on  
 315    flood depth may underestimate flood risk to vehicles. Past studies (Martinez-  
 316    Gomariz et al., 2018; Shand et al., 2011; Bocanegra et al., 2020) have de-  
 317    veloped stability criteria to identify dangerous roads by considering vehicle  
 318    characteristics and flood conditions (primarily flood depth and flow veloc-  
 319    ity). In the stability-centric approach, OpenSafe Mobility uses flood depth  
 320    over roads ( $d^r$ ) and flow velocity ( $v$ ) estimates from the flood model to iden-  
 321    tify unsafe roads for a vehicle class. Any stability criteria that quantify  
 322    vehicle stability using flood depth and flow velocity can be adopted in Open-  
 323    Safe Mobility. Fig. 5i-k (and Equation 3) show example stability criteria  
 324    ( $S^{dv}$ ) from the Australian Rainfall and Runoff (AR&R)(Shand et al., 2011)  
 325    for three classes of vehicles—small passenger cars, large passenger cars, and  
 326    large 4WD vehicles.

$$S^{dv}(d^r, v) = \begin{cases} safe, & \text{if } d^r \cdot v \leq s^v \text{ and} \\ & d^r \leq d^{max} \text{ and} \\ & v \leq v^{max} \\ unsafe, & \text{otherwise} \end{cases} \quad (3)$$

327    where:

- 328     $d^{max}=0.3\text{m}$ ;  $v^{max}=3\text{m/s}$ ;  $s^v=0.3\text{m}^2/\text{s}$  for small passenger cars;  
 329     $d^{max}=0.4\text{m}$ ;  $v^{max}=3\text{m/s}$ ;  $s^v=0.45\text{m}^2/\text{s}$  for large passenger cars; and  
 330     $d^{max}=0.5\text{m}$ ;  $v^{max}=3\text{m/s}$ ;  $s^v = 0.6\text{m}^2/\text{s}$  for large 4WD vehicles.

331 Fig. 5 shows an example road condition map using the three proposed  
332 strategies. Depth-based strategy is used to identify roads impassable (Fig.  
333 5b,d) for two vehicles with different wading heights (Fig. 5a,b). The prob-  
334 abilistic depth-based strategy is used to determine the probability of a road  
335 link being impassable (Fig. 5f,h) for two vehicle classes (Fig. 5e,g). Finally,  
336 AR&R stability criteria (Fig. 5i) is used to identify unsafe roads for small  
337 passenger cars (Fig. 5j) and large 4WD vehicles (Fig. 5k). The vehicle classes  
338 and their characteristics (safe wading height, wading height distribution, and  
339 stability criteria) are input to the OpenSafe Mobility framework; Fig. 5 il-  
340 lustrates some example vehicle classes and data that community members  
341 could use within the OpenSafe Mobility framework. Given information on  
342 vehicle characteristics, OpenSafe Mobility can estimate vehicle-specific road-  
343 link conditions.

344 Probabilistic depth-based criteria are suited for identifying potentially  
345 impassable roads and proactively initiating road closures by organizations  
346 responsible for managing flood response. Stability-based and depth-based  
347 strategies are ideal for identifying impassable roads considering individual  
348 vehicle characteristics and flow conditions. Here, vehicle-specific road condi-  
349 tion maps can be developed using vehicle-specific depth or stability (Martnez-  
350 Gomariz et al., 2017) criteria. Such maps are especially suited for emergency  
351 response vehicle selection and routing. While stability-based criteria are more  
352 comprehensive, it introduces additional computational cost for estimating  
353 flow velocity and consequently increases model runtime and time lag. The  
354 stability-based strategy should be preferred over the depth-based strategy,  
355 especially for regions that are predisposed to experience higher flow velocity

356 over roads during floods.

357 *2.4. Vehicle-Specific Network-Level Impacts of Flooding on Access to Select*  
358 *Facilities*

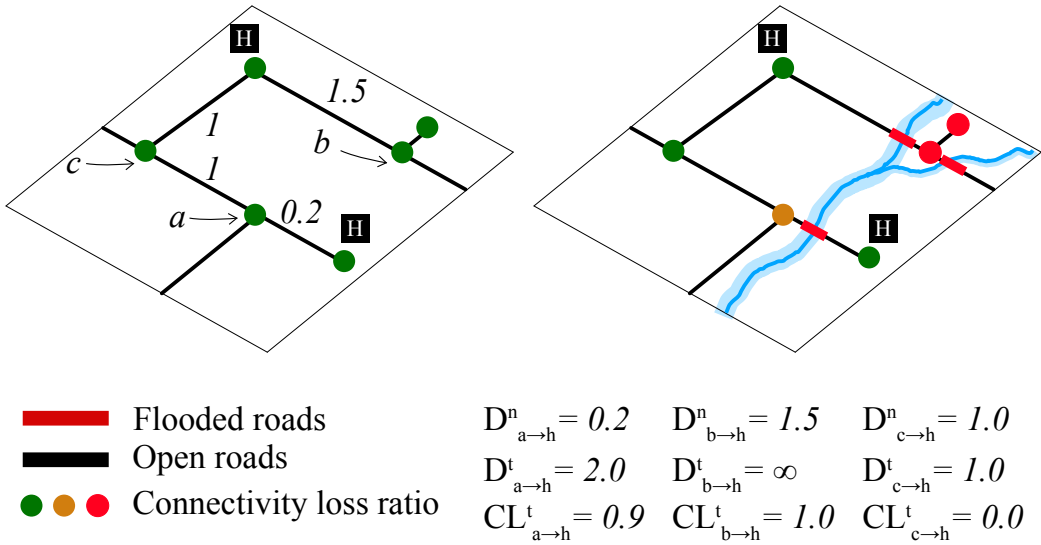
359 While identifying road conditions will facilitate safer mobility, link-level  
360 data alone is insufficient for emergency response situational awareness; identi-  
361 fying isolated regions with limited access to critical facilities such as hospitals,  
362 dialysis centers, fire stations, and evacuation routes are essential for prioritiz-  
363 ing emergency response. The network-level impacts can be quantified using  
364 real-time network analysis incorporating road conditions. The OpenSafe Mo-  
365 bility methodology for quantifying network-level impacts of flooding is shown  
366 in Fig. 6. First, the topology of the road network is represented as a graph  
367  $G = (V, E)$ , where  $V$  is a set of nodes representing points of interest such as  
368 road intersections and access locations, and  $E$  represents a set of road links  
369 connecting nodes. Next, baseline connectivity between every node in the  
370 network to the nearest facility is estimated for a select critical facility group  
371  $k$  (e.g., all hospitals). For example,  $D_{x \rightarrow k}^n$  represents the shortest distance  
372 between a node  $x$  to the nearest facility in  $k$  (e.g., the closest hospital) in the  
373 original road network. During flooding, impassable links ( $v_t^f$ ) and inundated  
374 nodes ( $e_t^f$ ) are removed to create an updated road network  $G_t^f = (V_t, E_t)$ ,  
375 where  $V_t = (V - v_t^f)$  and  $E_t = (E - e_t^f)$  at time  $t$ . The methodology to  
376 identify impassable links depends on the strategy adopted to determine road  
377 link status (Section 2.3). For the depth-centric strategy (Eq. 1), any closed  
378 roads (i.e.,  $R_d = \text{closed}$ ) are removed; for the stability-centric strategy (Eq.  
379 3), all unsafe roads (i.e.,  $S^{dv} = \text{unsafe}$ ) are removed. For the probabilis-  
380 tic depth-centric strategy (Eq. 2), a threshold probability of the link being

381 impassable for a select vehicle class (say, 5%) is chosen, and any road links  
382 that exceed the selected threshold are removed (i.e., links with  $P^d \geq 5\%$  are  
383 removed).

384 After removing impassable roads, the updated network is used to estimate  
385 the shortest distance ( $D_{x \rightarrow k}^t$ ) between node  $x$  to the nearest facility in  $k$  at  
386 time  $t$  (Dijkstra, 1959). Next, connectivity loss ( $CL_{x \rightarrow k}^t$ ) ratio (Gori et al.,  
387 2020), defined as  $1 - D_{x \rightarrow k}^n / D_{x \rightarrow k}^t$  for facility  $k$  and node  $x$  at time  $t$ , is  
388 used to quantify flood impact on access to the facility group  $k$ .  $CL_{x \rightarrow k}^t$  ratio  
389 varies between 0 and 1, with zero denoting no impact of flooding on the  
390 network access and one denoting complete loss of access. Finally, the node-  
391 level results can be aggregated at a geographical unit level, such as Census  
392 Tracts, to visualize the spatial distribution of flood impacts on access to a  
393 facility type. Connectivity loss maps can be generated for various critical  
394 facilities such as fire stations, dialysis centers, and shelter locations; such  
395 maps can provide a comprehensive view of flood impact on network access  
396 and assist decision-makers in identifying vulnerable regions and prioritizing  
397 emergency response actions. Finally, the OpenSafe Mobility framework can  
398 be easily extended to consider other accessibility measures (Faturechi and  
399 Miller-Hooks, 2015).

400 *2.5. Communication and Integration with Existing Intelligent Transportation  
401 Systems*

402 OpenSafe Mobility outputs include flood inundation maps, road condi-  
403 tions for different classes of vehicles, and the spatial distribution of flood  
404 impacts on access to select critical facilities such as evacuation routes, hospi-  
405 tals, pharmacies, and fire stations. These results are published via a website



$D_{X \rightarrow h}^n =$  Dist. from node X to the nearest hospital under normal condition  
 $D_{X \rightarrow h}^t =$  Dist. from node X to the nearest hospital under current condition  
 $CL_{X \rightarrow h}^t =$  Connectivity loss ratio of point X for hospitals ( $1 - D_{X \rightarrow h}^n / D_{X \rightarrow h}^t$ )

Figure 6: The methodology used to quantify network level impact of flooding on access to critical facilities. Here, connectivity loss ratio is used to quantify flood impact on access between nodes in the network to the nearest critical facility.

406 to facilitate easy access to stakeholders (Fig. 1e). In addition to providing a  
407 stand-alone website, OpenSafe Mobility also aims to augment existing situational  
408 awareness tools and intelligent transportation systems. Towards that  
409 goal, the OpenSafe Mobility framework also provides REST API access to  
410 the generated results (Fig. 1e). Any existing or future tools could acquire  
411 real-time georeferenced results from OpenSafe Mobility thorough REST API  
412 calls. By interfacing with existing situational awareness tools OpenSafe Mo-  
413 bility can significantly enhance situational awareness during flooding and  
414 facilitate safer mobility.

415 Table 1 summarizes the input data needed for the OpenSafe Mobility  
416 framework and example data sources. Before deploying OpenSafe Mobility,  
417 it is essential to identify the data and stakeholder needs as well as to develop  
418 and test flood and network analysis models.

### 419 **3. Experimental Evaluation**

420 This section presents the experiments designed to validate OpenSafe Mo-  
421 bility and critically evaluate it for strengths and limitations. A case study  
422 OpenSafe Mobility framework is deployed for the Brays Bayou Watershed  
423 area in Houston, Texas. The deployed framework is then evaluated using  
424 select recent historical storm events in the watershed. For each storm event,  
425 OpenSafe Mobility model predictions are compared to ground observations  
426 to quantify model performance. The following subsections describe the ex-  
427 perimental design in detail.

Table 1: Summary of input data required for the OpenSafe Mobility framework

Component	Data	Example data source or comment
<b>Radar Rainfall Data and Initialization</b>		
Acceptable time lag		Based on stakeholder need (e.g., $\leq 30$ min)
Flood inducing rainfall threshold		Based on hydrological studies (Dao et al., 2020), or historical data, or precipitation frequency estimates (Perica et al., 2018)
Maximum considered duration ( $d_{max}$ )		Based on model runtime and stakeholder needs (e.g., 8 days )
Computation resources		Stakeholder input
Rainfall data (GARR)		NEXRAD; Vieux & Associates, Inc.
<b>Hydrological and Hydraulic Modeling</b>		
Model building	Terrain data	Houston-Galveston Area Council (2022); U.S. Geological Survey (2023)
	Land use data	National Land Cover Database (NLCD) (Wickham et al., 2021)
	Soil data	Soil Survey Geographic Database (SSURGO) (Natural Resources Conservation Service, 2023)
	Bathymetry	Survey data (e.g., available in the hydraulic models from Harris County Flood Control District (2022b))
Model testing	Historical storms	NEXRAD; Vieux & Associates, Inc.; Iowa State University (2022); Harris County Flood Control District (2022a)
	Flood observations	Newspaper; social media; City of Houston (2022); Harris County Flood Control District (2022a); U.S. Geological Survey (2022b); TranStar (2022)
<b>Flood Impacts at the Road-Link Level</b>		
Road network	Road data	OpenStreetMap contributors (2017)
	Digital Surface Model	Houston-Galveston Area Council (2022)
Vehicle data	Vehicle database	Stakeholder input
	Safe wading height	Stakeholder input; owners manuals; Kramer et al. (2016)
	Wading height dist.	Stakeholder input; Contreras-Jara et al. (2018)
	Stability criteria	Martnez-Gomariz et al. (2018); Shand et al. (2011); Bocanegra et al. (2020)
<b>Flood Impact at the Road-Network Level</b>		
Census tract		U.S. Census Bureau (2022)
Location of select critical facilities		U.S. Department of Homeland Security (2022)
<b>Communication and Integration with Existing Tools</b>		
Web-hosting, cloud storage, and REST API		Amazon Web Services, Google Cloud Platform, etc.

428    *3.1. Study Area*

429    Houston, and specifically the Brays Bayou Watershed, is an ideal region  
430    for a case study of OpenSafe Mobility. Houston's location in the hurricane-  
431    prone Gulf of Mexico region, flat topography with little relief features (Se-  
432    bastian et al., 2017), insufficient storm drainage network capacity (Haddock  
433    and Kanwar, 2021), lack of zoning laws (Sebastian et al., 2017), rapid ur-  
434    banization (Zhang et al., 2018), and land-use change (Fang et al., 2014;  
435    Sebastian et al., 2017) renders it amongst the most vulnerable urban re-  
436    gions in the world (Chakraborty et al., 2019) for flooding. The flood risk  
437    was evident during several recent storms that wreaked havoc, especially to  
438    the transportation network. Any disturbance to the transportation network  
439    is especially detrimental to Houstonian's access to medical facilities concen-  
440    trated in the Texas Medical Center (TMC) region. The TMC, the world's  
441    largest medical center, sites a majority of health care facilities and is located  
442    in the Brays Bayou Watershed in Houston. Historically, the TMC facilities  
443    were either damaged (Fang et al., 2014) or lost connectivity to flooded re-  
444    gions (Gori et al., 2020) during major storms. Since situational awareness  
445    information related to healthcare access is critical for emergency response,  
446    Brays Bayou Watershed, which includes the TMC region, is selected for the  
447    case study.

448    Brays Bayou Watershed ( $329 \text{ km}^2$  or 127 square miles) is a densely popu-  
449    lated area southwest of Downtown Houston (Fig. 7). Brays Bayou, the main  
450    channel, begins in Fort Bend County and meets the Houston Ship Channel  
451    near Downtown Houston. The banks of Brays Bayou and its tributaries are  
452    highly developed and densely populated. Due to impervious surfaces and

453 concrete lined channels, the watershed is prone to flash flooding, posing a  
454 significant risk to the transportation infrastructure. Consequently, the wa-  
455 tershed was flooded during Tax Day flood (2016), Hurricane Harvey (2017),  
456 Tropical Storm (TS) Imelda (2019), and TS Beta (2020).

457 *3.2. Flood Events and Experiment Design*

458 Ideally, a situational awareness framework should be deployed first, and  
459 the long-term performance should be assessed through successive storms. In  
460 the absence of past performance data, this study will reenact four storms in  
461 OpenSafe Mobility and quantify model performance by comparing OpenSafe  
462 Mobility predictions to the recorded ground conditions. The selected storms  
463 are the Tax Day Flood (2016), Hurricane Harvey (2017), TS Imelda (2019),  
464 and TS Beta (2020). Hurricane Harvey's unprecedented rainfall intensity,  
465 duration, and spatial extent; Imelda's signature tri-peak pattern; and Beta  
466 and Tax Day Flood's flash flooding all pose unique challenges for situational  
467 awareness frameworks. Testing OpenSafe Mobility's efficacy during these  
468 storms facilitates a critical examination of its performance.

469 The Tax Day Flood (16-17 April 2016) (Nielsen and Schumacher, 2020)  
470 was a flash-flood-inducing high-intensity, short-duration event that hit south-  
471 eastern Texas. Several areas of Harris County received up to 400 mm of rain.  
472 The ensuing flooding damaged more than 10,000 homes and 40,000 vehicles.  
473 The second case study storm, Hurricane Harvey (25 August to 2 September  
474 2017) (Blake and Zelinsky, 2018) was a slow-moving hurricane that hovered  
475 near the Houston region for days, resulting in record-breaking rainfall. Un-  
476 precedented floods followed and damaged more than 300,000 structures and  
477 500,000 cars. Importantly, the inundated roadways and the paucity of real-

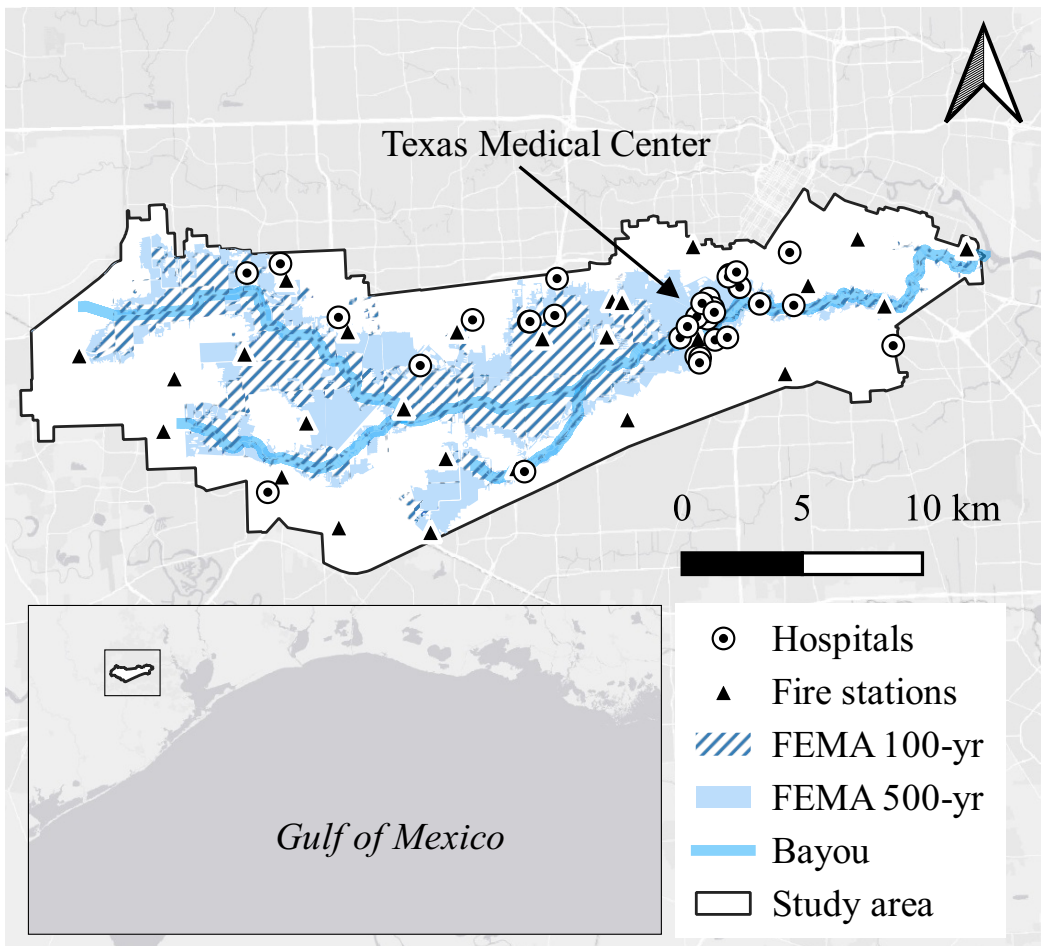


Figure 7: The study area, Brays Bayou Watershed, Houston, Texas, with the 100-year and 500-year flood plains. The 500-year flood plain represents an area with a 0.2 percent annual probability of flood exceedance. Many critical facilities such as hospitals and fire stations are located within the 500-year flood plain. Data sources: Esri (2022), FEMA (2022), U.S. Department of Homeland Security (2022), and Harris County Flood Control District (2022b).

478 time information on road network conditions crippled emergency response  
479 operations. The third storm, TS Imelda (17-20 September 2019) (Latto and  
480 Berg, 2020), dropped significant rain over various portions of Houston, al-  
481beit it was less intense than Harvey in the Houston area. More than 8200  
482 homes and 4500 roads were flooded, resulting in \$5 billion in losses. Finally,  
483 TS Beta (21-25 September 2020) (Beven and Berg, 2021) is the most recent  
484 among case study events. Beta was not as intense as the other case study  
485 storms, but it still caused more than \$225 million in damages.

486 The four case study storms are used to design three sets of experiments.  
487 In the first experiment, a flood model named *M1* is calibrated on Tax Day  
488 Flood and validated for Hurricane Harvey. In the second experiment, a new  
489 flood model *M2* is calibrated using Tax Day Flood and Hurricane Harvey  
490 and validated using TS Imelda and Beta. In the last experiment, Model *M3*  
491 is calibrated using all four storms in order to produce a robust model capable  
492 of handling a variety of future storms. The model *M3* is then deployed to  
493 perform real-time analysis in the watershed since September 2021. Model  
494 calibration mainly consisted of adjusting overland and channel Mannings *n*  
495 values. Additionally, changes to the mesh/grid were also made during cali-  
496 bration, such as adjusting the cell size and alignment. The calibration of the  
497 model occurs prior to its use in the framework. The model is calibrated for  
498 each experiment only using the data available before the validation storm,  
499 assuring temporally consistent experiments. The only exception is the use of  
500 the updated 2018 LiDAR instead of 2008 LiDAR data for *M1* and *M2* mod-  
501 els. Brays Bayou Watershed went through significant structural changes due  
502 to Project Brays—a watershed redevelopment program from Harris County

503 (Harris County Flood Control District, 2022c). Neglecting these changes  
504 could produce incorrect model results.

505 *3.3. Physics-Based Flood Models*

506 This study utilizes HEC-RAS version 6.0, which conducts hydrologic and  
507 hydraulic calculations in one with its 2D rain-on-grid functionality. The  
508 2D model takes input spatiotemporal rainfall data and calculates the water  
509 surface elevation and flow velocity data necessary for determining road condi-  
510 tions. A 2D model was chosen for this study due to its ability to capture both  
511 fluvial (riverine) and pluvial (local) flooding. Additionally, the 2D hydraulics  
512 are unsteady (rather than steady-state), allowing the model to account for  
513 any complex hydraulics or backwater effects arising from the flat topography  
514 of the bayou. To model the hydrologic process, rainfall and infiltration data  
515 are required. Gage-adjusted radar rainfall data at the subbasin level was used  
516 for Hurricane Harvey, TS Imelda, and TS Beta and was obtained from Vieux  
517 & Associates, Inc. (2022). For the Tax Day Flood, gage-adjusted Next Gen-  
518 eration Weather Radar (NEXRAD) (Iowa State University, 2022) was used  
519 and is provided at the  $1 \text{ km}^2$  resolution. To model infiltration, soil data from  
520 the Natural Resources Conservation Service at a resolution of 30m x 30m was  
521 utilized and the Green & Ampt infiltration method was selected. Model pa-  
522 rameters used were based off the HEC-RAS manual (Brunner, 2021) as well  
523 as from Harris County Flood Control District's (HCFCD) HEC-HMS model  
524 (Harris County Flood Control District, 2022b). Additionally, imperviousness  
525 data was included in the model at the subbasin level, with imperviousness  
526 values taken from HCFCD's HEC-HMS model.

527 The basis for hydraulic modeling in HEC-RAS 6.0 2D is a computational

mesh, terrain, and land use data. The mesh consists of mainly 137 m x 137 m (450 ft x 450 ft) squares, except in channel areas, where the mesh is refined to contain roughly 30.5 m x 30.5 m (100 ft x 100 ft) cells. HEC-RAS does not treat each cell as having a single elevation but is instead able to capture the underlying terrain in each cell, creating detailed elevation volume/area relationships of each cell. The faces of each cell are essentially treated as cross-sections in that detailed elevation versus area, wetted perimeter, and roughness relationships are defined for each face of each cell (Brunner, 2021). This allows larger cell sizes to be used without compromising accuracy or resolution, thereby lowering the computational time. The boundary conditions for the 2D area are based on normal depth conditions. Land use data at a resolution of 30m x 30m was obtained from the 2016 National Land Cover Database (NLCD) (Wickham et al., 2021) and provides the basis for Manning's n values, which relate surface roughness to flow rate. While the NLCD also provides 2019 land use data, 2016 data was selected to better match the calibration events. Because Brays is already highly developed, there is negligible difference in the two datasets. 2018 HGAC LiDAR (Houston-Galveston Area Council, 2022) data was used for the terrain data set. Since LiDAR data is unable to capture channel bathymetry well, cross-section elevation data from HCFCD's current HEC-RAS model of Brays (Harris County Flood Control District, 2022b) was interpolated in the channel and used instead of LiDAR data in the channel.

OpenSafe Mobility's ability to detect road conditions throughout the watershed depends on the performance of the flood model to capture both pluvial and fluvial flooding. The model calibration and validation for fluvial

553 flooding is shown in Appendix A and demonstrated acceptable accuracy (for  
554 example, the Nash-Sutcliffe Model Efficiency Coefficient for validating Hur-  
555 ricane Harvey exceeded .85 at all gages). Further, the main sections of the  
556 paper focus on validating pluvial flooding (for inferring roadway conditions  
557 away from the bayous) and road conditions.

558 *3.4. Spatial Model Performance*

559 Model performance for pluvial floods is quantified by comparing OpenSafe  
560 Mobility model predictions to flood observations from the City of Houston  
561 (CoH) 311 data (City of Houston, 2022). Residents can report flooding and  
562 request services like debris removal through the City of Houston's citizen  
563 service portal. The spatial location and the reported time of these flood  
564 reports are used in this experiment to validate OpenSafe Mobility.

565 Fig. 8a depicts the temporal distribution of 311 flood reports during  
566 Hurricane Harvey. Fig. 8b-d present the spatial distribution of the 311  
567 flood data with the flood inundation map for that time step from *M1*. Fig.  
568 8e shows the spatial distribution of all flood reports from 311 data (385  
569 observations) for Hurricane Harvey. Similarly, Fig. 8f-j show 311 data (29  
570 observations) for TS Imelda and model predictions from *M2*, while Fig. 8k-o  
571 show 311 data (32 observations) from TS Beta and model predictions from  
572 *M2*.

573 For each flood report in the 311 data, the most recent depth map is  
574 used to infer the condition within a buffer radius of the flood report. A  
575 buffer radius is used as many 311 locations are geocoded using standardized  
576 addresses, and in many cases, residents will report street flooding even when  
577 their parcel is not flooded. Streets are susceptible to flooding due to the

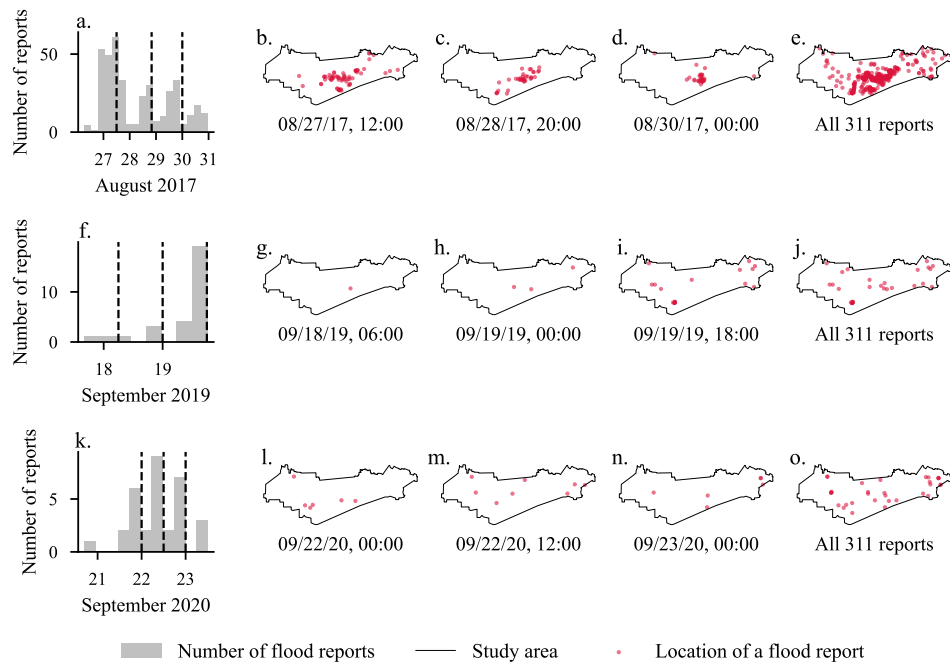


Figure 8: Location of flood reports from 311 call database. Parts a, f, and k show the temporal distribution of flood reports during Hurricane Harvey, Tropical Storm Imelda, and Tropical Storm Beta. Parts b-d show the location of flood reports for three timestamps and Part e shows all flood reports for the event duration. Data sources: City of Houston (2022) and Harris County Flood Control District (2022b).

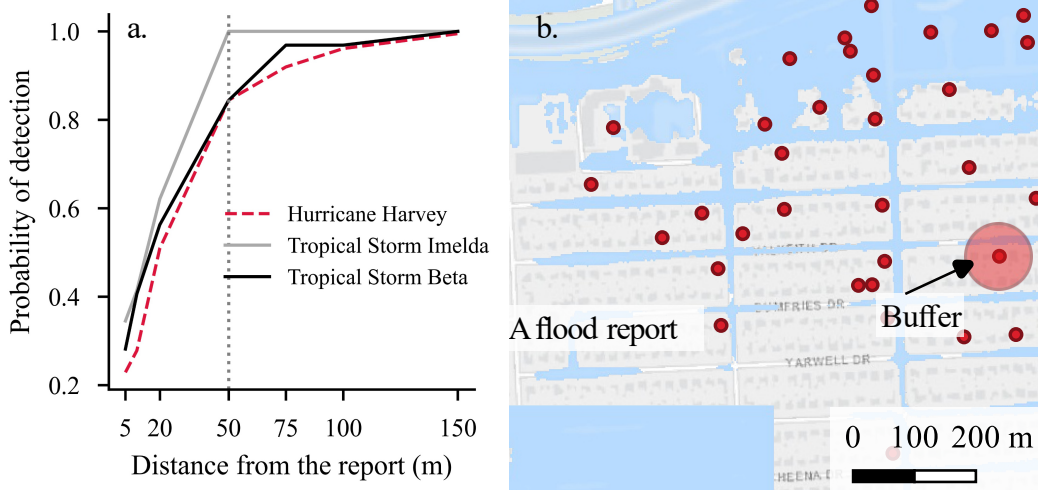


Figure 9: OpenSafe Mobility model performance for detecting flooding for three case study storms. Results indicate that OpenSafe Mobility can reliably capture spatial distribution of flooding. Data sources: Esri (2022) and City of Houston (2022).

578 clogging of stormwater networks and their lower elevation compared to the  
 579 adjacent regions. Fig. 9b shows an example buffer around a flood report. It  
 580 is evident that though the reported location is dry, the adjoining street is  
 581 flooded.

582 Probability of detection (PoD) is used to measure model performance in  
 583 this experiment and is the proportion of actual flooded cases (311 reports)  
 584 that the model correctly identified. PoD ranges from 0 to 1, and a higher  
 585 value indicates superior model performance. The PoD of a model depends on  
 586 the buffer distance. For example, in Fig. 9a, as the buffer distance increases  
 587 from 5 m to 150 m, the PoD increases from 20 percent to 100 percent. Study-  
 588 ing model performance indicates that in all three flood events, OpenSafe Mo-  
 589 bility could detect flooding for at least 80 percent of the cases within a buffer  
 590 of 50 m. Further, for a buffer of 150 m, the models could detect flooding for

591 nearly all 311 reports. Further visual inspection reveals that false-negative  
592 flood reports at a buffer typically represent scenarios where flooded locations  
593 are encoded using conventional addresses adjacent to a flooded street. This  
594 experiment demonstrates OpenSafe Mobility’s capacity to model fluvial and  
595 pluvial flooding reliably.

596 *3.5. Quantitative Model Performance*

597 This section assesses OpenSafe Mobility’s ability to provide reliable water  
598 depth estimates by comparing OpenSafe Mobility model predictions to traf-  
599 fic camera data (Fig. 10) and USGS high water level marks (HWLMs) (Fig.  
600 11). HWLMs report the maximum water level observed at points without  
601 information on observation time. In contrast, while traffic camera data from  
602 Houston TranStar provides the observation time, it doesn’t give a quantita-  
603 tive estimate of flood depth, necessitating qualitative flood depth inference  
604 from images.

605 Fig. 10 compares the flood depth estimates from traffic cameras to Open-  
606 Safe Mobility ( $M_1$  for Hurricane Harvey;  $M_2$  for TS Imelda and Beta) flood  
607 estimates at the time of observation. Flood depths from images are esti-  
608 mated by comparing the flooded scene to its normal dry condition. Due to  
609 the inability to determine an exact flood depth, a most likely value (repre-  
610 sented by a dot) and the lower and upper bounds of flood depths (repre-  
611 sented by error bars) are reported. The results for Hurricane Harvey (mean  
612 error (ME) = 0.16, mean absolute error (MAE)=0.48, root mean square  
613 error (RMSE)=0.74 (Botchkarev, 2019) for 10 observations) indicate that  
614 for Harvey, the OpenSafe Mobility model provides a reasonable estimate  
615 of flood depth. Here, mean error (ME) is defined as  $1/n \sum_{j=1}^n e_j$  where

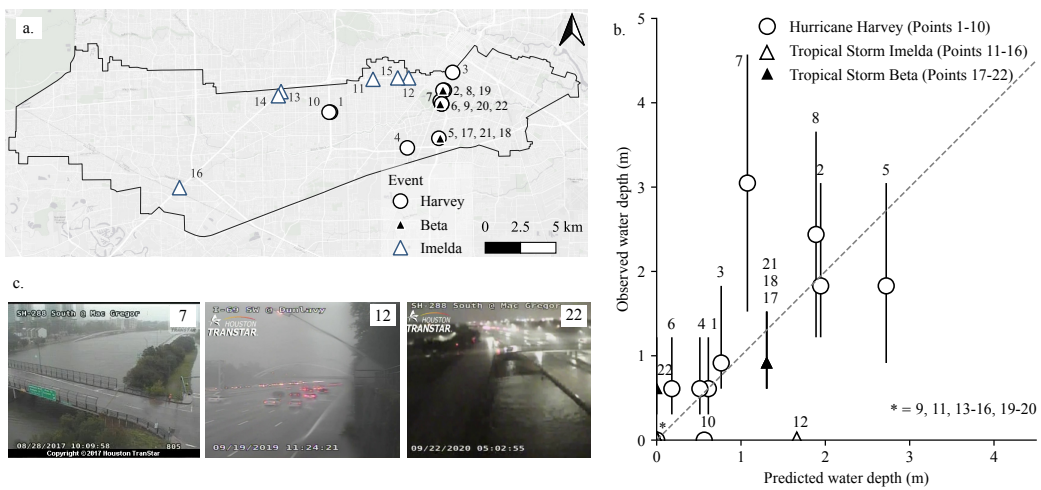


Figure 10: Comparisons of observed flood depths from traffic camera data to OpenSafe Mobility model predictions. Part a maps the locations of the traffic camera data; part b compares the flood depth estimated from images to OpenSafe Mobility predictions; and part c offers some example traffic camera images. Error bars (part b) represent potential lower and upper bounds in the depth estimate from images, while numbers (parts a, b, c) identify data points. Data sources: Harris County Flood Control District (2022b); TranStar (2022).

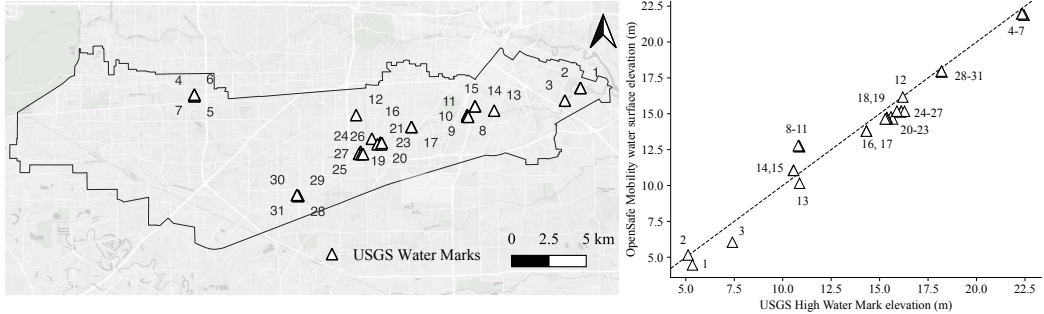


Figure 11: Comparison of observed USGS high water level marks with OpenSafe Mobility model predictions for Hurricane Harvey. Numbers locate data points on the map. Data sources: U.S. Geological Survey (2022a); Harris County Flood Control District (2022b).

*e<sub>j</sub> = A<sub>j</sub> - P<sub>j</sub>*,  $A_j$  is the observed value,  $P_j$  is the model predicted value, and  $n$  is the number of observations. Similarly, mean absolute error (MAE) is defined as  $1/n \sum_{j=1}^n |e_j|$  and root mean square error (RMSE) is defined as  $\sqrt{1/n \sum_{j=1}^n e_j^2}$ . It can also be noted that OpenSafe Mobility model predictions slightly underestimate flood depths. Further, visual inspection of the data indicates that the model predictions are within the observed range of values for 7 out of 10 flood observations. Similarly, Fig. 11 plots the USGS High Water Level Marks (HWLMs) with water surface elevation from OpenSafe Mobility. Comparison results (ME=0.21, MAE=0.77, RMSE=0.93 for 31 observations) indicate a similar model performance as the camera data. These results show that OpenSafe Mobility can provide flood depth estimates with reasonable accuracy and identify flooded roads.

In both Imelda and Beta, no widespread flooding was observed in the study region. For TS Imelda (ME=-0.27, MAE=0.27, RMSE=0.68 for 6 observations), the model (*M2*) correctly predicts all cases except one (Fig. 10-b (point 12)), where OpenSafe Mobility overestimates the flood depth on

632 a portion of Interstate-69 that is flanked by elevated embankments, resulting  
633 in a deep, channel-like topography. This error demonstrates the model's  
634 inability to account for artificial drainage systems. Likewise for TS Beta,  
635 OpenSafe Mobility (*M*2) overestimated flood depth at three locations along  
636 the SH288 highway as demonstrated by the results (ME=-0.09, MAE=0.30,  
637 RMSE=0.38 for 6 observations). This may be due to the fact that for small  
638 events such as Imelda and Beta, storm networks are effective in reducing  
639 the intensity of flooding. Since OpenSafe Mobility cannot currently model  
640 storm networks, it overestimates the flood depth. Despite these limitations,  
641 OpenSafe Mobility provided flood depth estimates with reasonable accuracy  
642 for most locations tested. Further, locations where the model will fail are  
643 predictable based on the topography.

644 *3.6. An Overview of OpenSafe Mobility Results for Hurricane Harvey*

645 This section evaluates OpenSafe Mobility's capacity to identify flooded  
646 roads and contrasts it to the Texas Department of Transportation (TxDOT)  
647 flood closure reports. Further, it also demonstrates OpenSafe Mobility's  
648 ability to quantify link and network-level flood impacts considering vehicle  
649 characteristics and roadway topography. This validation exercise is limited  
650 to the Hurricane Harvey case study since only Hurricane Harvey had any  
651 notable network-wide impact on roads in the study region. Fig. 12-1a locates  
652 all flood reports from TxDOT (Texas Department of Transportation, 2022)  
653 in the study region during Hurricane Harvey. Similarly, Fig. 12-1b-e show  
654 the temporal evolution of flooding using closure reports from TxDOT. A  
655 closer examination of the TxDOT data reveals that all closed roads are not  
656 flooded. The TxDOT data, for example, shows that the whole Interstate-610

loop around Houston is closed due to floods. While portions of Interstate-610 were flooded, the loop as a whole was not flooded but was closed to the public. As a result, a direct comparison of TxDOT data with OpenSafe Mobility reports may not be fully appropriate; however the comparison is made herein for insights on roadway level performance.

Fig. 12-2a-e show flood reports from OpenSafe Mobility for passenger cars. For identifying flooded roads, see the methodology described in Section 2.3. For Fig. 12-2a-i, a wading height of 0.5 m is used to identify roads flooded for passenger cars. Fig. 12-2a shows the collection of all roads impacted at any time during Harvey. Comparing Fig. 12-2a with Fig. 12-1a highlights the increase in data availability using OpenSafe Mobility compared to TxDOT. Fig. 12-2b-e show the evolution of roadway flooding at different time steps during Harvey. Further, Fig. 12-2f-i show the evolution of access to hospitals quantified using connectivity loss (*CL*) ratio. *CL* ratio is estimated by performing network analysis on the updated network without flooded roads at any time step. The regions with severe connective loss might have limited access to hospitals using passenger cars with wading height 0.5m or less.

Similarly, Fig. 12-3a-i show the road condition and network-level impacts for high water vehicles. Here, a 1.2 m (4 ft) wading height is used to identify flooded roads and quantify network-level impacts. It is important to notice that many roads flooded for passenger cars are open for high water trucks; consequently, many regions inaccessible via a passenger car are accessible to high water trucks. This illustrates the importance of considering vehicle characteristics while identifying flood impacts. Furthermore, sites inaccessi-

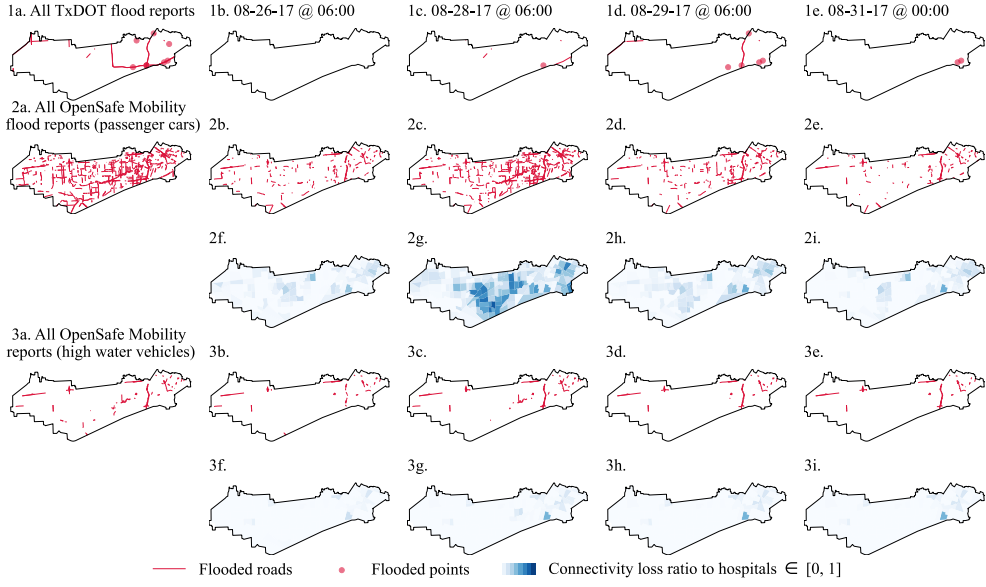


Figure 12: Comparison of flood observations from TxDOT and results from OpenSafe Mobility at various time steps. OpenSafe Mobility can provide vehicle class-specific road trafficability data as well as assess the accessibility to select facilities. A depth-centric approach is used here to identify flooded roads. A road is considered closed for a vehicle if the water depth over the road exceeds the safe wading height. A safe wading height of 0.5 m is considered for passenger cars (parts 2a-i) and 1.2m for high-water vehicles (3a-i). The first column reports flooded roads at any time during Hurricane Harvey, and the remaining columns represent conditions at select time steps indicated in the first row (parts 1b-e). Data sources: Texas Department of Transportation (2022), Harris County Flood Control District (2022b), and OpenStreetMap contributors (2017).

ble to high-water trucks necessitate specialized equipment, such as boats, to carry out any emergency response operation.

Fig. 13-a-i illustrate a probabilistic approach to quantify flood impact on roads. Here, a normal distribution ( $\mathcal{N}(0.4125\text{m}, 0.0232\text{m})$ ) (Contreras-Jara et al., 2018) is used to model the wading height of passenger cars. Given flood depths at roads, the probability of a road being impassable is the probability of wading height less than the flood depth. Fig. 13-a depicts the maximum probability of roads being impassable at any time throughout the storm. Fig. 13-b-e show the temporal evolution of the probability of roads being impassable for the select vehicle class. The probability of road closure data will aid decision-makers in deciding road closure decisions and managing risk. For example, a traffic information system can tag any roads with a probability of flooding greater than a threshold, such as 5%, as flooded. Further, emergency responders can identify flooded roads and inaccessible regions based on risk tolerance and available equipment. For example, Fig. 13-f-i show access to hospitals considering only roads with a 95% probability of remaining open.

Fig. 14-1a-i and Fig. 14-2a-i illustrate the stability-centric approach to identify flooded roads. Fig. 14-1a and 2a show any road that experienced unsafe conditions for small passenger cars and large 4WD vehicles following AR&R criteria. Fig. 14-1b-e and Fig. 14-2b-e identify unsafe roads, and Fig. 14-1f-i and Fig. 14-2f-i quantify network level impacts of road closures on access to hospitals for small passenger and large 4WD vehicles respectively.

These validation case studies showcased the capacity of OpenSafe Mobility to provide reliable estimates of link and network-level impacts of flood-

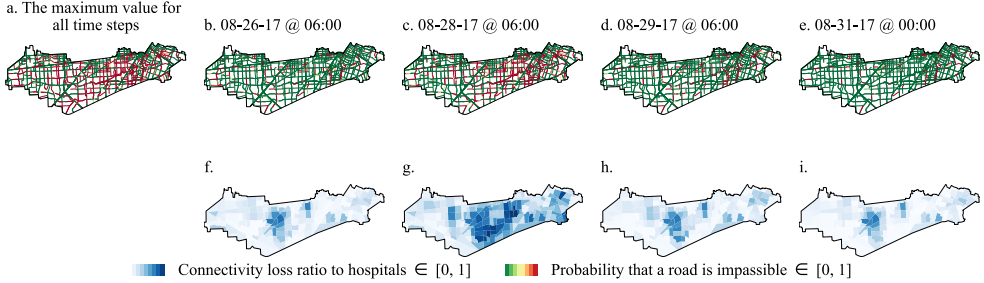


Figure 13: The probabilistic depth-centric approach for estimating road link conditions and network-level impacts of flooding. Here, a wading height distribution for passenger cars and water depth over roads are used to infer the probability of road links being impassable (parts a-e). Access to hospitals (parts f-i) is then evaluated only considering road links with a 95% probability of remaining open. The first column depicts the maximum probability of roads being impassable at any time during Hurricane Harvey, and the remaining columns represent conditions at select time steps indicated in the first row (parts b-e). Data sources: Harris County Flood Control District (2022b) and OpenStreetMap contributors (2017).

ing. OpenSafe Mobility significantly advances the state-of-the-art situational awareness frameworks focused on mobility. Continued validation can occur as data is collected and the framework is tested in an online deployment.

#### 4. Deployment

A prototype of the OpenSafe Mobility framework has been operational since 8 Sept 2021. In this limited deployment, OpenSafe Mobility is run on a local workstation (Intel Core i7-4790 CPU @3.60 GHz and 16 GB RAM). Python packages are used to process radar rainfall (Basyal, 2022), automate HEC-RAS runs (Dysarz, 2018), perform network (Hagberg et al., 2008) and spatial analyses (Jordahl et al., 2020). The M3 version of the model is used with gauge-adjusted radar rainfall data from Vieux & Associates, Inc. The

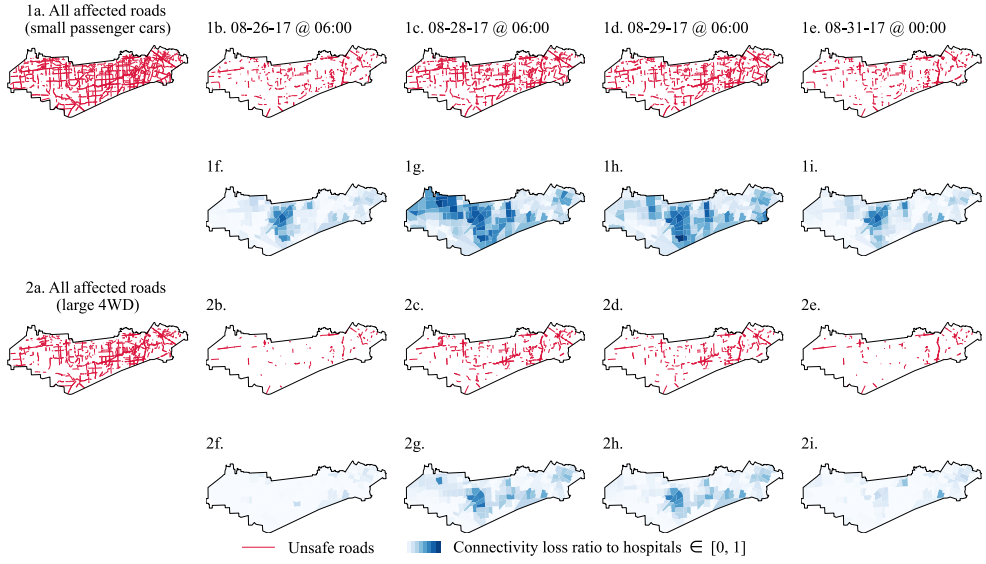


Figure 14: The stability-centric approach for estimating road link conditions and network-level impacts of flooding. Here, AR&R stability criteria are used to identify unsafe roads for small passenger cars (parts 1a-e) and large 4WD vehicles (parts 2a-e). Access to hospitals is then evaluated only considering safe roads for small passenger cars (parts 1f-i) and large 4WD vehicles (parts 2f-i). The first column reports unsafe road links at any time during Hurricane Harvey, and the remaining columns represent conditions at select time steps indicated in the first row (parts 1b-e). Data sources: Texas Department of Transportation (2022), Harris County Flood Control District (2022b), OpenStreetMap contributors (2017), and U.S. Department of Homeland Security (2022).

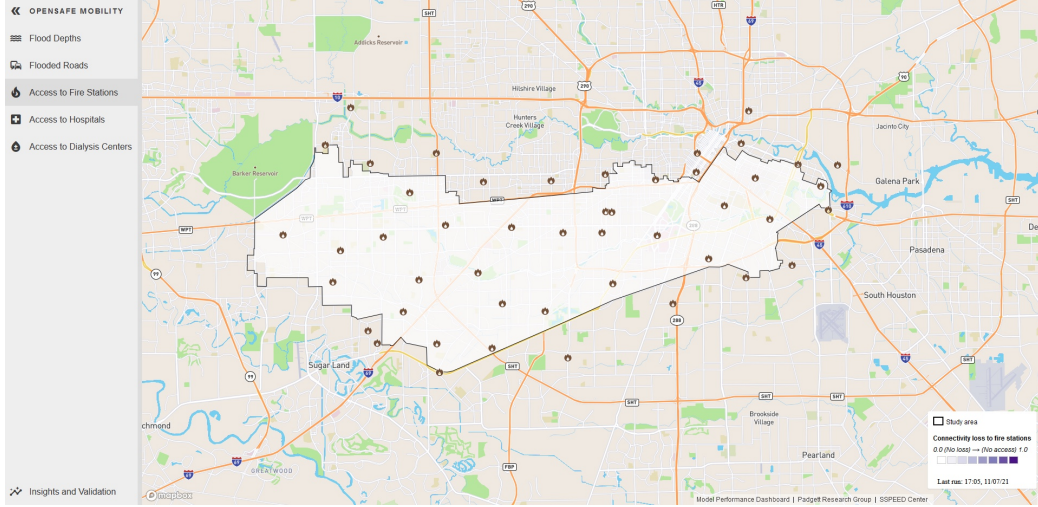


Figure 15: Screenshot of the OpenSafe Mobility website.

preceding eight days of rainfall data ( $d_{max} = 8$  days) are used to model current flood conditions at each time step. The results are then uploaded to Amazon Simple Storage Service. Finally, the results are published using a website developed using HTML, JavaScript, CSS, and Mapbox. Currently, the OpenSafe Mobility website (Fig. 15) is hosted on Amazon Web Services and can be accessed at [www.opensafemobility.com](http://www.opensafemobility.com). The typical time lag is between 10 and 28 minutes, which includes the time it takes to acquire (5-18 minutes) and process the gage-adjusted radar data (< 1min), run the flood model (2-10 minutes), perform network and spatial analysis (3-4 minutes), and publish the results (< 1 min).

Since the model's deployment, no major flood events have occurred in the study region. As a result, the model's performance cannot be assessed further at this point. However, for reliable stakeholder dependent deployment two limitations of the system architecture should be addressed in the long

732 term. These include the need for hosting on multiple computers that are not  
733 co-located with the study region. Additionally, future deployments would  
734 ideally leverage multiple data sources, as the current system relies on a single  
735 radar data source.

736 **5. Discussion**

737 *5.1. OpenSafe Mobility Framework and Case Studies*

738 This paper proposed a new situational awareness framework for nowcast-  
739 ing road network conditions during flooding. It combined a state-of-the-art  
740 flood model, widely available gage-adjusted radar rainfall data, and network  
741 and spatial analyses using open-source tools and data to infer vehicle-class  
742 specific road conditions and community access. A case study analysis then  
743 evaluated the nowcasting model for Brays Bayou Watershed in Houston,  
744 Texas. The case study used four recent storms in the watershed and tested  
745 the ability of OpenSafe Mobility to sense the flooding using quantitative and  
746 qualitative metrics.

747 Finally, it is essential to note that OpenSafe Mobility does not identify  
748 flooded roads to facilitate routing over flooded streets. Instead, it seeks to  
749 identify open roads to support routing, reduce delays and detours, and en-  
750 hance roadway safety. It also aims to support decision-making by identifying  
751 affected regions and aiding emergency response vehicle selection to access  
752 isolated neighborhoods. While limitations certainly exist in the flood depth  
753 predictions due to the numerical nature of the hydraulic model and uncer-  
754 tainties associated with modeling large storm events, the validation exercises  
755 prove that OpenSafe Mobility can sense flood impact on road networks and

756 aid in identifying open roads for emergency vehicles.

757 *5.2. Assumptions and Limitations*

758 Case studies highlight several limitations of the OpenSafe Mobility frame-  
759 work. HEC-RAS 6.0, and consequently OpenSafe Mobility, cannot model the  
760 underground drainage network and as such, pluvial flooding is overestimated.  
761 However, because Houston's drainage network is only designed to handle a  
762 2-year storm (Haddock and Kanwar, 2021)(50% annual chance), and because  
763 OpenSafe Mobility is only triggered with a higher threshold event (say 5-year  
764 event or greater), the overestimation of flood extents is limited. During large  
765 storm events, the drainage system is overwhelmed and therefore the assump-  
766 tion made in this methodology is reasonable that the runoff will mostly  
767 remain overland and not be funneled into culverts and underground pipes.  
768 The lack of underground drainage modeling can also lead to an underesti-  
769 mation of fluvial flooding, as water that is normally routed into bayous via  
770 underground networks are not being modeled. Therefore, a more accurate  
771 model would be able to account for underground drainage, either by deduct-  
772 ing a 2-year rainfall from the input rainfall, or by using a model that accounts  
773 for underground drainage (BMT Commercial Australia Pty Ltd, 2022) (al-  
774 though the latter can be infeasible and time-consuming for watershed-scale  
775 modeling).

776 Additionally, pumping systems that play a critical role in pumping water  
777 out of low spots on freeways were not modeled. This was due to a lack of  
778 information about these pumps (such as flow rate) as well as the modeling  
779 difficulties that arise when pumps are introduced (such as model instability).  
780 Because of this, OpenSafe Mobility displays flooding at freeway underpasses

781 that otherwise may have been pumped out. Like the underground drainage  
782 system, these pumps can be overwhelmed in large storms events, which makes  
783 our lack of pumps a reasonable assumption. However, as seen with the  
784 validation and calibration results, a model that performs well for a longer  
785 duration storm event (such as Hurricane Harvey) may not perform as well  
786 for a shorter storm event (such as TS Beta). Additionally, a model that  
787 performs well for a single-peak event (such as the Tax Day flooding) did not  
788 perform as well for the triple-peak event of TS Imelda. To account for this  
789 variability, future versions of OpenSafe Mobility could consider deploying  
790 different models depending on storm characteristics.

791 *5.3. Transferability and Scalability*

792 OpenSafe Mobility might be transferrable to other regions for which re-  
793 liable data is available for replicating the framework. Data needs and exam-  
794 ple data sources for OpenSafe Mobility are listed in Table 1. Rainfall data  
795 sources that can be used in OpenSafe Mobility, whether rain gage data or  
796 radar data, are widely available. Some examples are NEXRAD (for the US)  
797 and Operational Programme for the Exchange of Weather Radar Informa-  
798 tion (for Europe). Further, several existing methodologies and open source  
799 tools exist in the literature to facilitate fusion of gage data and radar data  
800 to generate GARR. While the case studies presented in the paper only used  
801 GARR to validate OpenSafe Mobility performance, rain gage or radar data  
802 could also be used. Since the accuracy of rainfall data will affect the reliabil-  
803 ity of OpenSafe Mobility results, any future deployment should test model  
804 performance using the adopted rainfall source(s). Other data required for  
805 flood modeling, such as the terrain, land cover data, imperviousness data,

806 and bathymetry data, are widely available and commonly used in hydrologic  
807 and hydraulic models. Similarly, data for network and spatial analyses can  
808 be obtained from OpenStreetMaps and the census department. For deploy-  
809 ment, the OpenSafe Mobility web framework uses HTML, CSS, JavaScript,  
810 and Mapbox. While Mapbox is not open source, similar functionality can  
811 be replicated using Leaflet—an open-source JavaScript library. All codes  
812 required to implement the OpenSafe Mobility are available in the project’s  
813 GitHub repository (Panakkal et al., 2022). OpenSafe Mobility may be trans-  
814 ferable to communities with access to hydrologic and hydraulic models and  
815 reliable input data (Table 1); however, significant investments may be re-  
816 quired for areas without access to accurate data and models.

817 *5.4. Future Opportunities*

818 OpenSafe Mobility provides a deterministic prediction of flooding. Flood-  
819 ing involves complex interactions between the built environment and water,  
820 and a probabilistic model may be better suited to provide a holistic rep-  
821 resentation of flood hazards. Running a suite of flood models instead of a  
822 single model used in OpenSafe Mobility can effectively provide a probability  
823 measure of flood hazard, albeit engendering considerable computation and  
824 processing costs. Surrogate models based on deep learning that can lever-  
825 age GPUs offer a promising approach to enable real-time probabilistic flood  
826 inundation mapping. OpenSafe Mobility can be further improved by aug-  
827 menting it with other data sources such as traffic cameras and official traffic  
828 alerts. For example, traffic cameras overlooking potential ponding locations  
829 can be used to adjust OpenSafe Mobility predictions and correct for over-  
830 estimation of flooding in such regions. Further, OpenSafe Mobility doesn’t

831 currently attempt to forecast road conditions; instead, it's designed to de-  
832 tect current flood conditions on the road after rainfall has occurred within  
833 an acceptable time lag. Recent advances in radar nowcasting (Ravuri et al.,  
834 2021) can be used in the future to forecast road conditions. Future studies  
835 should also test the transferability and scalability of the OpenSafe Mobility  
836 framework to different regions with diverse topography, situational aware-  
837 ness needs, and data availability. Finally, the current version of OpenSafe  
838 Mobility did not consider systemic stakeholder needs assessment and instead  
839 concentrated on methodological aspects; future versions and deployments of  
840 OpenSafe Mobility should be co-developed with stakeholders following the  
841 tenets of user-centered design principles (Robinson et al., 2005).

842 *5.5. Key Contributions in the Context of Existing Frameworks*

843 OpenSafe Mobility advances the current state-of-the-art by providing  
844 vehicle-specific road condition and network impact data at high spatial and  
845 temporal resolution and with limited time lag and bias compared to most  
846 existing situational awareness tools. Similar to frameworks leveraging phys-  
847 ical water level sensors, OpenSafe Mobility can provide inundation depth to  
848 support decision making considering vehicle characteristics. Although less  
849 accurate than water level sensors, the low cost and high availability coupled  
850 with an acceptable accuracy make OpenSafe Mobility a good candidate to  
851 complement depth sensors. Ideally such sensors should be sited in regions  
852 where the accuracy of OpenSafe Mobility is limited. Further, OpenSafe Mo-  
853 bility provides a competent alternative to social sensors; especially, it pro-  
854 vides a source devoid of biases in social sensors, provides quantitative flood  
855 depth estimates, and can match or exceed the availability of social sensors.

856 When compared to remote sensors (e.g., satellite images, UAVs), OpenSafe  
857 Mobility provides quantitative water depth estimates with limited time lag  
858 and is not affected by factors such as cloud or vegetation cover.

859 Next, OpenSafe Mobility enables equitable access to situational awareness  
860 data for flood-prone communities. Flood-prone communities with access to  
861 data and models required for OpenSafe Mobility can leverage the framework  
862 to aid decision-making and situational awareness, making it a sustainable,  
863 low-cost alternative to costly options such as physical sensors.

864 Finally, this study advances the current state-of-the-art for using flood  
865 models to infer flood impacts on roads in real time. Specifically, the re-  
866 sults show that a multi-disciplinary approach integrating radar rainfall data,  
867 physics-based flood models, vehicle characteristics, roadway topography, and  
868 network and spatial analyses can provide high-resolution information on flood  
869 impact on transportation networks. The proposed framework distinguishes  
870 itself from the existing flood model-based frameworks (Panakkal et al., 2019;  
871 Mioc et al., 2015; Ming et al., 2020; Naulin et al., 2013; Versini et al., 2010;  
872 Morsy et al., 2018) in terms of its focus on roadway mobility (especially in  
873 terms of vehicle-specific road link- and network-level impacts), consideration  
874 of flood mechanism (enabling it to infer the conditions of roads away from  
875 the streams), roadway topography (allowing it to capture roadway elevation),  
876 and vehicle stability. Further, the study highlighted the limitations of the  
877 proposed model and suggested future work to address them.

878 **6. Conclusions**

879 Reliable nowcasting of roadway conditions during flooding is a long-  
880 standing challenge with societal importance for emergency response and road-  
881 way safety. Our approach using radar rainfall data and a physics-based flood  
882 model directly addresses this vital problem and provides current informa-  
883 tion on connectivity to critical facilities. We showed using case studies that  
884 the proposed framework offers improved nowcasting of roadway conditions.  
885 Primarily, it can provide high-resolution data on local roads and vehicle  
886 class-specific road condition data needed for vehicle and route selection for  
887 emergency response. The real-time convergence of flood estimation with the  
888 vehicle-specific link- and network-level analyses distinguishes OpenSafe Mo-  
889 bility as a unique mobility-centric framework that addresses the growing need  
890 to sense road conditions during flooding. Further, while not attempted in  
891 this paper, the proposed framework might be transferable to other regions  
892 with access to reliable hydrologic and hydraulic models and real-time rainfall  
893 data. Any implementation of OpenSafe Mobility should be tailored to the  
894 data availability in the study region and undergo extensive testing before  
895 widespread adoption. While continued development and extensive testing  
896 under diverse storms and data availability are still required, OpenSafe Mo-  
897 bility has the potential to augment existing ITS tools and equip emergency  
898 managers and responders with a holistic picture of flood impact on mobility  
899 and community access.

900 Yet, there remain further challenges to be addressed in our nowcasting  
901 framework. As case studies demonstrated, OpenSafe Mobility provides reli-  
902 able flood impact prediction during major floods, but modeling the impact

903 of stormwater networks and pumping stations remains difficult. Critically,  
904 OpenSafe Mobility could overestimate flooding in regions with efficient ar-  
905 tificial drainage systems. Future versions of OpenSafe Mobility will address  
906 this challenge by integrating stormwater networks in hydraulic and hydrologic  
907 models and leveraging information from other sources such as traffic cameras  
908 using data fusion. Another important challenge not discussed in this study  
909 is the scalability of the model to a large area. Implementing a model for a  
910 large urban area such as Greater Houston could increase model delay from  
911 under 30 minutes to over an hour. Such a high time lag is undesirable for  
912 situational awareness applications. Using a surrogate model to capture hy-  
913 drological and hydraulic models as an alternative to the physics-based flood  
914 model could reduce the time lag. Further, real-time network analysis for  
915 a large network requires leveraging recent developments in surrogate models  
916 (Stern et al., 2017) and network analysis (Leskovec and Sosić, 2016). Finally,  
917 OpenSafe Mobility uses a deterministic model to capture flooding; given the  
918 complexity of the flooding process, a probabilistic approach can be leveraged  
919 to account for uncertainties. Despite these shortcomings, OpenSafe Mobility  
920 provides a pathway to reliable situational awareness for communities.

## 921 Acknowledgments

922 This work was supported by the National Science Foundation (NSF)  
923 award numbers 1951821, 1842494, and 1545837. Authors would like to ac-  
924 knowledge the contributions of David Brooks (support with access to radar  
925 data), Matthew Garcia (guidance on flood modeling), Joe Hurley and Steven  
926 Michalek (support with access to TxDOT public data), and Rice University

927 GIS/Data Center (support with access to LiDAR open data). The authors  
928 thank the anonymous reviewers for their constructive feedback. Any opin-  
929 ions, findings, and conclusions or recommendations expressed in this paper  
930 are those of the authors and do not necessarily reflect the views of the spon-  
931 sors.

932 **Appendix A. Model Performance for Fluvial Flooding**

933 Fluvial validations are achieved by comparing observed and modeled tem-  
934 poral water surface elevations (WSE) at three United States Geological Sur-  
935 vey (USGS) gages along Brays. By visual inspection, a good validation is one  
936 that agrees well with observed data in both the peak and timing of the stage  
937 hydrograph. Quantitatively, validations are measured by the Nash-Sutcliffe  
938 Efficiency index (NSE) (Nash and Sutcliffe, 1970). NSE values range between  
939  $-\infty$  and 1, with 1 being an exact match to observed data, and negative values  
940 indicating that the average of the observed data would be a better fit than  
941 the modeled data.

942 As can be seen in Fig. A.16e-f, the model demonstrates a good fit qual-  
943 itatively (hydrograph timing and peak) for gages at Gessner Dr. and Main St.  
944 For the most upstream gage, Brays at Alief (Fig. A.16d), the model underes-  
945 timates peak WSE in the validation case despite a good match in hydrograph  
946 timing. However, the authors determined that this was a satisfactory valida-  
947 tion as most flooding in the watershed occurs further downstream than this  
948 gage, and the gages further downstream displayed good model performance.  
949 Further validation exercises continued to prove the validity of the model.  
950 As shown in Fig. A.17j-l, the model validation of Tropical Storm Beta

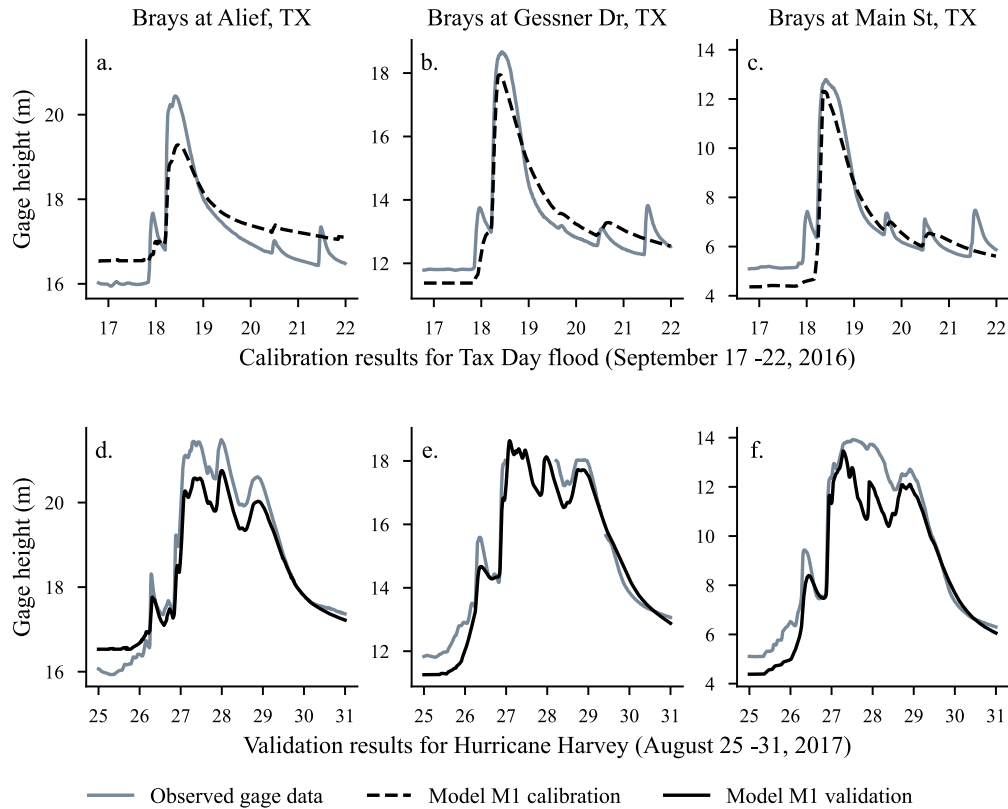


Figure A.16: Observed and predicted gage heights at three watchpoints along Brays Bayou. Model *M1* was calibrated on Tax Day flood (part a-c) and validated on Hurricane Harvey (part d-f). The results show good agreement between model prediction and observed rainfall during validation (part d-f). The broken line in part e indicates no data due to gage malfunction. Data source: U.S. Geological Survey (2022b).

951 matched in both hydrograph peak and timing. The validation of Tropi-  
952 cal Storm Imelda (Fig. A.17g-i) contained discrepancies in the falling limbs  
953 of the hydrographs, however, for this tri-peak storm, the timings and val-  
954 ues of peak WSEs were well-matched. The errors in the falling limb of this  
955 validation lead only to a conservative estimation of flooding by predicting  
956 a prolonged flooding. Therefore, the authors concluded a satisfactory vali-  
957 dation of *M2*. Model *M3* is validated on all four storms. The red dotted  
958 lines in Fig. A.17a-l display the *M3* calibration, which is the final calibration  
959 version of the model used in the deployment of OpenSafe Mobility. Overall,  
960 and especially for the two downstream gages of Gessner Dr. and Main St.,  
961 the model shows a satisfactory match to observed stage data.

962 The accuracy of a model can also be quantitatively measured using the  
963 NSE index. As the four validations storms were quite different in duration,  
964 intensities, total rainfall, and temporal patterns, it was a challenge to cre-  
965 ate a model that was robust in its applicability to various types of storms.  
966 However, using *M3*, which was calibrated using all four historical storms,  
967 the NSE values for all storms and at all gages are satisfactory, as shown  
968 in Table A.2. Notably, the gage at Gessner Dr. has good validations for  
969 all storms, which is important for this work as most flooding is observed in  
970 the area around this gage (the Meyerland area). Due to the good qualitative  
971 and quantitative validations of the model, it was adopted for predicting flood  
972 levels in OpenSafe Mobility.

973 Ahmad, K., Pogorelov, K., Riegler, M., Ostroukhova, O., Halvorsen, P.,  
974 Conci, N., Dahyot, R., 2019. Automatic detection of passable roads after

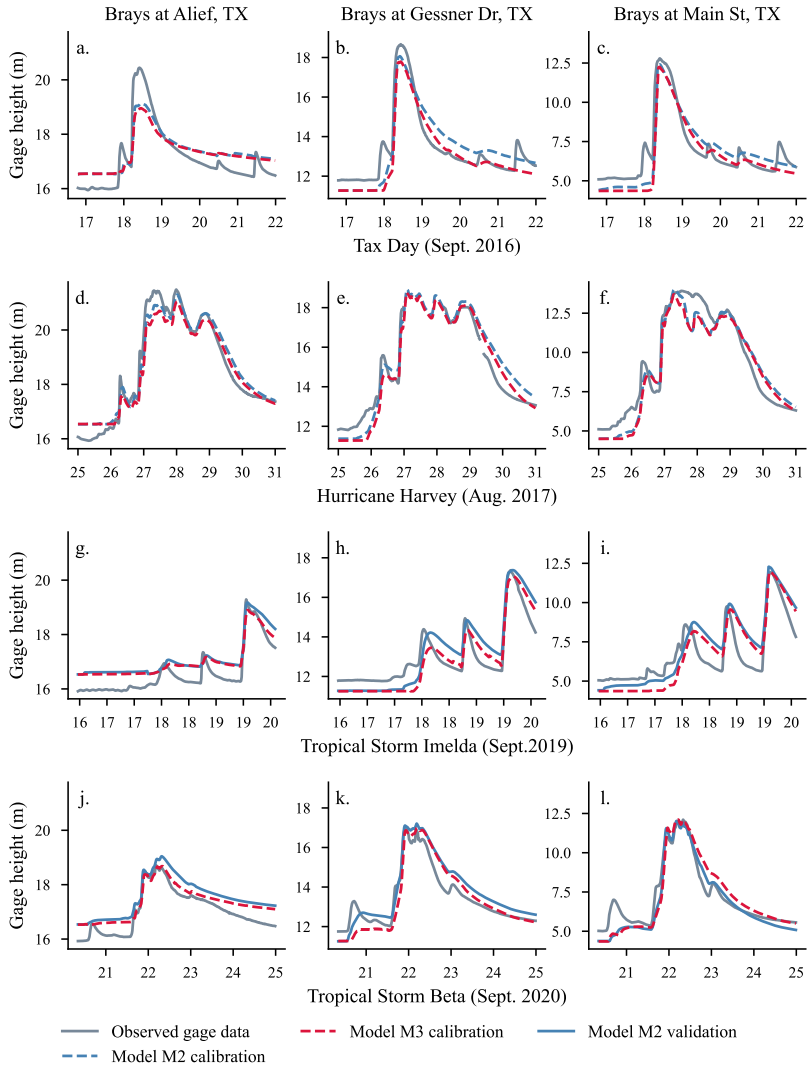


Figure A.17: Observed and predicted gage heights at three watchpoints along Brays Bayou for four case study storms. Model  $M_2$  was calibrated on Tax Day flood (part a-c) and Hurricane Harvey (part d-f) and validated on Tropical Storms Imelda (part g-i) and Beta (part j-l). Similarly, Model  $M_3$  was calibrated on all four storms. During the validation stage, Model  $M_2$  showed acceptable performance for unseen storms. Data source: U.S. Geological Survey (2022b).

Table A.2: Summary of model performance

Model	Gage	NashSutcliffe model efficiency coefficient <sup>1</sup>			
		Tax Day	Harvey	Imelda	Beta
<i>M1</i>	Alief	0.80	<b>0.92</b>		
	Gessner Dr.	0.95	<b>0.93</b>		
	Main St.	0.93	<b>0.88</b>		
<i>M2</i>	Alief	0.79	0.96	<b>0.60</b>	<b>0.53</b>
	Gessner Dr.	0.92	0.87	<b>0.70</b>	<b>0.82</b>
	Main St.	0.92	0.91	<b>0.64</b>	<b>0.89</b>
<i>M3</i>	Alief	0.75	0.94	0.68	0.76
	Gessner Dr.	0.93	0.89	0.79	0.82
	Main St.	0.91	0.90	0.63	0.83

<sup>1</sup> The results in normal font are calibration results and the results in the bold font are validation results. For example, Model *M1* was calibrated using Tax Day flood and validated on Hurricane Harvey. Similarly, Model *M2* was calibrated using Tax Day, Hurricane Harvey and validated on Tropical Storms Imelda and Beta.

- 975        floods in remote sensed and social media data. *Signal Processing: Image*  
976        *Communication* 74, 110–118. doi:10.1016/j.image.2019.02.002.
- 977        Basyal, G., 2022. Pydsstools. URL: <https://github.com/gyanz/pydsstools>. (Last Accessed: 2022-03-06).
- 979        Beven, J.L., Berg, R., 2021. Tropical Cyclone Report Tropical Storm Beta  
980        (AL222020) 1722 September 2020. Technical Report. National Hurricane  
981        Center.
- 982        Blake, E., Zelinsky, D., 2018. Tropical Cyclone Report Hurricane Harvey  
983        (AL092017) 17 August – 1 September 2017. Technical Report. National  
984        Hurricane Center.
- 985        BMT Commercial Australia Pty Ltd, 2022. TUFLOW. URL: <https://www.tuflow.com/>. (Last Accessed: 2022-01-04).
- 987        Bocanegra, R.A., Valls-Morn, F.J., Frans, F., 2020. Review  
988        and analysis of vehicle stability models during floods and pro-  
989        posal for future improvements. *Journal of Flood Risk Manage-  
990        ment* 13, e12551. URL: <https://onlinelibrary.wiley.com/doi/abs/10.1111/jfr3.12551>, doi:10.1111/jfr3.12551. eprint:  
992        <https://onlinelibrary.wiley.com/doi/pdf/10.1111/jfr3.12551>.
- 993        Botchkarev, A., 2019. Performance Metrics (Error Measures) in Machine  
994        Learning Regression, Forecasting and Prognostics: Properties and Typol-  
995        ogy. *Interdisciplinary Journal of Information, Knowledge, and Manage-  
996        ment* 14, 045–076. URL: <http://arxiv.org/abs/1809.03006>, doi:10.  
997        28945/4184. arXiv: 1809.03006.

- 998 Brunner, G.W., 2021. HEC-RAS River Analysis System 2D Modeling User's  
999 Manual Version 6.0 Beta. Technical Report CPD-68A. USACE Hydrologic  
1000 Engineering Center: Davis, CA, USA.
- 1001 Carreño Conde, F., De Mata Muñoz, M., 2019. Flood monitoring based on  
1002 the study of sentinel-1 sar images: The ebro river case study. Water 11,  
1003 2454.
- 1004 Chakraborty, J., Collins, T.W., Grineski, S.E., 2019. Exploring the Envi-  
1005 ronmental Justice Implications of Hurricane Harvey Flooding in Greater  
1006 Houston, Texas. American Journal of Public Health 109, 244–250.  
1007 doi:10.2105/AJPH.2018.304846. publisher: American Public Health As-  
1008 sociation.
- 1009 Chaudhary, P., DArongo, S., Moy de Vitry, M., Leito, J.P., Wegner, J.D.,  
1010 2019. Flood-Water Level Estimation from Social Media Images. ISPRS  
1011 Annals of the Photogrammetry, Remote Sensing and Spatial Information  
1012 Sciences IV-2/W5, 5–12. doi:10.5194/isprs-annals-IV-2-W5-5-2019.
- 1013 City of Houston, 2022. Houston, Texas 3-1-1. URL: [https://www.](https://www.houstontx.gov/311/)  
1014 [houstontx.gov/311/](https://www.houstontx.gov/311/). (Last Accessed: 2022-03-27).
- 1015 Coles, D., Yu, D., Wilby, R.L., Green, D., Herring, Z., 2017. Be-  
1016 yond flood hotspots: Modelling emergency service accessibility dur-  
1017 ing flooding in York, UK. Journal of Hydrology 546, 419–  
1018 436. URL: [https://www.sciencedirect.com/science/article/pii/](https://www.sciencedirect.com/science/article/pii/S0022169416308022)  
1019 S0022169416308022, doi:10.1016/j.jhydrol.2016.12.013.

- 1020 Contreras-Jara, M., Echaveguren, T., Vargas Baecheler, J., Chamorro Gin,  
1021 A., de Solminihac Tampier, H., 2018. Reliability-Based Estimation of  
1022 Traffic Interruption Probability due to Road Waterlogging. Journal of  
1023 Advanced Transportation 2018, e2850546. doi:10.1155/2018/2850546.  
1024 publisher: Hindawi.
- 1025 Dao, D.A., Kim, D., Kim, S., Park, J., 2020. Determination of flood-inducing  
1026 rainfall and runoff for highly urbanized area based on high-resolution radar-  
1027 gauge composite rainfall data and flooded area GIS data. Journal of Hy-  
1028 drology 584, 124704. doi:10.1016/j.jhydrol.2020.124704.
- 1029 De Longueville, B., Smith, R.S., Luraschi, G., 2009. ”OMG, from here, I  
1030 can see the flames!” a use case of mining location based social networks to  
1031 acquire spatio-temporal data on forest fires, in: Proceedings of the 2009  
1032 international workshop on location based social networks, pp. 73–80.
- 1033 Dey, K.C., Mishra, A., Chowdhury, M., 2015. Potential of Intelligent Trans-  
1034 portation Systems in Mitigating Adverse Weather Impacts on Road Mobil-  
1035 ity: A Review. IEEE Transactions on Intelligent Transportation Systems  
1036 16, 1107–1119. doi:10.1109/TITS.2014.2371455.
- 1037 Dijkstra, E.W., 1959. A note on two problems in connexion with graphs.  
1038 Numerische Mathematik .
- 1039 Dysarz, T., 2018. Application of Python Scripting Techniques for Control  
1040 and Automation of HEC-RAS Simulations. Water 10, 1382. doi:10.3390/  
1041 w10101382.

- 1042 Esri, 2022. Esri World Light Gray Base Map. URL: [http://services.arcgisonline.com/ArcGIS/rest/services/Canvas/World\\_Light\\_Gray\\_Base/MapServer/tile/%7Bz%7D/%7By%7D/%7Bx%7D](http://services.arcgisonline.com/ArcGIS/rest/services/Canvas/World_Light_Gray_Base/MapServer/tile/%7Bz%7D/%7By%7D/%7Bx%7D).  
1043  
1044 (Last Accessed: 2022-03-27).
- 1045  
1046 Evans, B., Chen, A.S., Djordjevi, S., Webber, J., Gmez, A.G., Stevens, J., 2020. Investigating the Effects of Pluvial Flooding and Climate Change on Traffic Flows in Barcelona and Bristol. Sustainability 12, 2330. URL: <https://www.mdpi.com/2071-1050/12/6/2330>, doi:10.3390/su12062330. number: 6 Publisher: Multidisciplinary Digital Publishing Institute.  
1047  
1048  
1049  
1050  
1051
- 1052 Fan, C., Esparza, M., Dargin, J., Wu, F., Oztekin, B., Mostafavi, A., 2020a. Spatial biases in crowdsourced data: Social media content attention concentrates on populous areas in disasters. Computers, Environment and Urban Systems 83, 101514. Publisher: Elsevier.  
1053  
1054  
1055
- 1056 Fan, C., Wu, F., Mostafavi, A., 2020b. A Hybrid Machine Learning Pipeline for Automated Mapping of Events and Locations From Social Media in Disasters. IEEE Access 8, 10478–10490. doi:10.1109/ACCESS.2020.2965550. conference Name: IEEE Access.  
1057  
1058  
1059
- 1060 Fang, Z., Bedient, P.B., Buzcu-Guven, B., 2011. Long-Term Performance of a Flood Alert System and Upgrade to FAS3: A Houston, Texas, Case Study. Journal of Hydrologic Engineering 16, 818–828. doi:10.1061/(ASCE)HE.1943-5584.0000374. publisher: American Society of Civil Engineers.  
1061  
1062  
1063
- 1064 Fang, Z., Dolan, G., Sebastian, A., Bedient, P.B., 2014. Case Study of Flood

- 1065 Mitigation and Hazard Management at the Texas Medical Center in the  
1066 Wake of Tropical Storm Allison in 2001. Natural Hazards Review 15,  
1067 05014001. doi:10.1061/(ASCE)NH.1527-6996.0000139. publisher: Amer-  
1068 ican Society of Civil Engineers.
- 1069 Faturechi, R., Miller-Hooks, E., 2015. Measuring the Performance of Trans-  
1070 portation Infrastructure Systems in Disasters: A Comprehensive Review.  
1071 Journal of Infrastructure Systems 21, 04014025. doi:10.1061/(ASCE)IS.  
1072 1943-555X.0000212. publisher: American Society of Civil Engineers.
- 1073 FEMA, 2022. FEMA Flood Map Service Center. URL: <https://msc.fema.gov/portal/home>. (Last Accessed: 2022-03-27).
- 1074
- 1075 Field, C.B., Barros, V., Stocker, T.F., Dahe, Q., 2012. Managing the risks of  
1076 extreme events and disasters to advance climate change adaptation: spe-  
1077 cial report of the intergovernmental panel on climate change. Cambridge  
1078 University Press.
- 1079 Geetha, M., Manoj, M., Sarika, A.S., Mohan, M., Rao, S.N., 2017. Detec-  
1080 tion and estimation of the extent of flood from crowd sourced images, in:  
1081 2017 International Conference on Communication and Signal Processing  
1082 (ICCSP), IEEE. pp. 0603–0608.
- 1083 Google LLC, 2022a. Driving directions, live traffic & road conditions updates.  
1084 URL: <https://www.waze.com/live-map/>. (Last Accessed: 2022-03-18).
- 1085 Google LLC, 2022b. Material Icons Guide | Google Fonts. URL: [https://developers.google.com/fonts/docs/material\\_icons](https://developers.google.com/fonts/docs/material_icons). accessed Au-  
1086 gust 25, 2022.
- 1087

- 1088 Gori, A., Gidaris, I., Elliott, J.R., Padgett, J., Loughran, K., Bedient, P.,  
1089 Panakkal, P., Juan, A., 2020. Accessibility and Recovery Assessment of  
1090 Houstons Roadway Network due to Fluvial Flooding during Hurricane  
1091 Harvey. Natural Hazards Review 21, 04020005. doi:10.1061/(ASCE)NH.  
1092 1527-6996.0000355. publisher: American Society of Civil Engineers.
- 1093 Green, D., Yu, D., Pattison, I., Wilby, R., Bosher, L., Patel, R., Thomp-  
1094 son, P., Trowell, K., Draycon, J., Halse, M., Yang, L., Ryley, T.,  
1095 2017. City-scale accessibility of emergency responders operating dur-  
1096 ing flood events. Natural Hazards and Earth System Sciences 17, 1–16.  
1097 URL: <https://nhess.copernicus.org/articles/17/1/2017/>, doi:10.  
1098 5194/nhess-17-1-2017. publisher: Copernicus GmbH.
- 1099 Guerrero-Ibez, J., Zeadally, S., Contreras-Castillo, J., 2018. Sensor Tech-  
1100 nologies for Intelligent Transportation Systems. Sensors 18, 1212. doi:10.  
1101 3390/s18041212.
- 1102 Hackl, J., Lam, J.C., Heitzler, M., Adey, B.T., Hurni, L., 2018. Es-  
1103 timating network related risks: A methodology and an application in  
1104 the transport sector. Natural Hazards and Earth System Sciences 18,  
1105 2273–2293. URL: <https://nhess.copernicus.org/articles/18/2273/2018/>, doi:10.5194/nhess-18-2273-2018. publisher: Copernicus GmbH.
- 1107 Haddock, C., Kanwar, S., 2021. Infrastructure Design Manual  
1108 2021. Technical Report. City of Houston, Houston Public Works.  
1109 Houston. URL: <https://parkusa.com/index.php/files/132/SW-Harris-County---COH/384/COH-Infrastructure-Design-Manual.pdf>.

- 1112 Hagberg, A., Swart, P., S Chult, D., 2008. Exploring network structure,  
1113 dynamics, and function using NetworkX. Technical Report. Los Alamos  
1114 National Lab.(LANL), Los Alamos, NM (United States).
- 1115 Han, Z., Sharif, H.O., 2021. Analysis of Flood Fatalities in the United States,  
1116 19592019. Water 13, 1871. doi:10.3390/w13131871. number: 13 Publisher:  
1117 Multidisciplinary Digital Publishing Institute.
- 1118 Harris County Flood Control District, 2022a. Harris County Flood Warn-  
1119 ing System. URL: <https://www.harriscountyfws.org/>. (Last Accessed:  
1120 2022-03-18).
- 1121 Harris County Flood Control District, 2022b. Model and Map Man-  
1122 agement (M3) System. URL: <https://www.hcfcd.org/Resources/Interactive-Mapping-Tools/Model-and-Map-Management-M3-System>.  
1123 (Last Accessed: 2022-03-04).
- 1125 Harris County Flood Control District, 2022c. Project Brays Features. URL:  
1126 <https://www.hcfcd.org/Activity/Active-Projects/Brays-Bayou/C-11-Project-Brays/Project-Brays-Features>. (Last Accessed:  
1127 2022-03-04).
- 1129 He, X., Lu, D., Margolin, D., Wang, M., Idrissi, S.E., Lin, Y.R., 2017. The  
1130 signals and noise: actionable information in improvised social media chan-  
1131 nels during a disaster, in: Proceedings of the 2017 ACM on web science  
1132 conference, pp. 33–42.
- 1133 Houston-Galveston Area Council, 2022. LiDAR Imagery | Houston-

- 1134 Galveston Area Council (H-GAC). URL: <https://www.h-gac.com/imagery/lidar>. (Last Accessed: 2022-03-04).
- 1135
- 1136 Iowa State University, 2022. MRMS data archive. URL: <https://mtarchive.geol.iastate.edu/>. (Last Accessed: 2022-03-06).
- 1137
- 1138 Jiang, J., Liu, J., Qin, C.Z., Wang, D., 2018. Extraction of Urban Waterlogging Depth from Video Images Using Transfer Learning. *Water* 10, 1485.
- 1139
- 1140 doi:10.3390/w10101485. number: 10 Publisher: Multidisciplinary Digital
- 1141 Publishing Institute.
- 1142 Johnson, J.M., Coll, J.M., Ruess, P.J., Hastings, J.T., 2018. Challenges and
- 1143 Opportunities for Creating Intelligent Hazard Alerts: The FloodHippo
- 1144 Prototype. *Journal of the American Water Resources Association* 54,
- 1145 872–881. URL: <https://onlinelibrary.wiley.com/doi/abs/10.1111/1752-1688.12645>, doi:10.1111/1752-1688.12645.
- 1146
- 1147 Johnson, J.M., Munasinghe, D., Eyelade, D., Cohen, S., 2019. An
- 1148 integrated evaluation of the National Water Model (NWM)Height
- 1149 Above Nearest Drainage (HAND) flood mapping methodology.
- 1150 *Natural Hazards and Earth System Sciences* 19, 2405–2420.
- 1151 URL: <https://nhess.copernicus.org/articles/19/2405/2019/>,
- 1152 doi:10.5194/nhess-19-2405-2019.
- 1153 Jongman, B., Ward, P.J., Aerts, J.C.J.H., 2012. Global exposure to river and
- 1154 coastal flooding: Long term trends and changes. *Global Environmental*
- 1155 *Change* 22, 823–835. doi:10.1016/j.gloenvcha.2012.07.004.

- 1156 Jonkman, S.N., 2007. Loss of life estimation in flood risk assessment; theory  
1157 and applications. Ph.D. thesis. TU Delft.
- 1158 Jordahl, K., den Bossche, J.V., Fleischmann, M., Wasserman, J., McBride,  
1159 J., Gerard, J., Tratner, J., Perry, M., Badaracco, A.G., Farmer, C., et al.,  
1160 2020. geopandas/geopandas: v0.8.1. URL: <https://doi.org/10.5281/zenodo.3946761>, doi:10.5281/zenodo.3946761.
- 1162 Kramer, M., Terheiden, K., Wiprecht, S., 2016. Safety criteria for  
1163 the trafficability of inundated roads in urban floodings. International Journal of Disaster Risk Reduction 17, 77–84. URL: <https://linkinghub.elsevier.com/retrieve/pii/S2212420915301783>, doi:10.  
1164 1016/j.ijdrr.2016.04.003.
- 1167 Landuyt, L., Van Wesemael, A., Schumann, G.J.P., Hostache, R., Verhoest,  
1168 N.E., Van Coillie, F.M., 2018. Flood mapping based on synthetic aperture  
1169 radar: An assessment of established approaches. IEEE Transactions on  
1170 Geoscience and Remote Sensing 57, 722–739.
- 1171 Latto, A., Berg, R., 2020. Tropical Cyclone Report Tropical Storm Imelda  
1172 (AL112019) 1719 September 2019. Technical Report. National Hurricane  
1173 Center.
- 1174 Leskovec, J., Sosić, R., 2016. SNAP: A general-purpose network analysis  
1175 and graph-mining library. ACM Transactions on Intelligent Systems and  
1176 Technology (TIST) 8, 1–20.
- 1177 Levy, B.S., Patz, J.A., 2015. Climate Change, Human Rights, and Social

- 1178        Justice. Annals of Global Health 81, 310. doi:10.1016/j.aogh.2015.08.  
1179                  008.
- 1180        Lo, S.W., Wu, J.H., Lin, F.P., Hsu, C.H., 2015. Visual Sensing for Urban  
1181                  Flood Monitoring. Sensors 15, 20006–20029. doi:10.3390/s150820006.  
1182                  number: 8 Publisher: Multidisciplinary Digital Publishing Institute.
- 1183        Maples, L.Z., Tiefenbacher, J.P., 2009. Landscape, development, technology  
1184                  and drivers: The geography of drownings associated with automobiles in  
1185                  Texas floods, 19502004. Applied Geography 29, 224–234. doi:10.1016/j.  
1186                  apgeog.2008.09.004.
- 1187        Martnez-Gomariz, E., Gmez, M., Russo, B., Djordjevi, S., 2017. A  
1188                  new experiments-based methodology to define the stability thresh-  
1189                  old for any vehicle exposed to flooding. Urban Water Journal 14,  
1190                  930–939. URL: <https://www.tandfonline.com/doi/full/10.1080/1573062X.2017.1301501>. doi:10.1080/1573062X.2017.1301501.
- 1192        Martnez-Gomariz, E., Gmez, M., Russo, B., Djordjevi, S., 2018. Stability  
1193                  criteria for flooded vehicles: a state-of-the-art review: Stability criteria for  
1194                  flooded vehicles. Journal of Flood Risk Management 11, S817–S826. URL:  
1195                  <https://onlinelibrary.wiley.com/doi/10.1111/jfr3.12262>, doi:10.  
1196                  1111/jfr3.12262.
- 1197        Ming, X., Liang, Q., Xia, X., Li, D., Fowler, H.J., 2020. Real-  
1198                  Time Flood Forecasting Based on a High-Performance 2-D Hydrody-  
1199                  namic Model and Numerical Weather Predictions. Water Resources

- 1200 Research 56, e2019WR025583. doi:10.1029/2019WR025583. eprint:  
1201 <https://onlinelibrary.wiley.com/doi/pdf/10.1029/2019WR025583>.
- 1202 Mioc, D., Nkhwanana, J., Moreiri, K., Nickerson, B., Santos, M.,  
1203 McGillivray, E., Morton, A., Anton, F., Ahmad, A., Mezouaghi, M., Mof-  
1204 ford, L., Tang, P., 2015. Natural and man-made flood risk mapping and  
1205 warning for socially vulnerable populations. International Journal of Safety  
1206 and Security Engineering 5, 183–202. doi:10.2495/SAFE-V5-N3-183-202.
- 1207 Morsy, M.M., Goodall, J.L., O’Neil, G.L., Sadler, J.M., Voce, D., Hassan, G.,  
1208 Huxley, C., 2018. A cloud-based flood warning system for forecasting im-  
1209 pacts to transportation infrastructure systems. Environmental Modelling  
1210 & Software 107, 231–244. doi:10.1016/j.envsoft.2018.05.007.
- 1211 Mudashiru, R.B., Sabtu, N., Abustan, I., Balogun, W., 2021. Flood hazard  
1212 mapping methods: A review. Journal of Hydrology 603, 126846. doi:10.  
1213 1016/j.jhydrol.2021.126846.
- 1214 Nash, J., Sutcliffe, J., 1970. River flow forecasting through conceptual models  
1215 part I A discussion of principles. Journal of Hydrology 10, 282–290.  
1216 doi:10.1016/0022-1694(70)90255-6.
- 1217 National Oceanic and Atmospheric Administration, 2016. National water  
1218 model: Improving noaas water prediction services. URL: <https://water.noaa.gov/documents/wrn-national-water-model.pdf>.
- 1219  
1220 National Weather Service, 2022. National Weather Service Radar. URL:  
1221 <https://radar.weather.gov>. (Last Accessed: 2021-06-16).

- 1222 Natural Resources Conservation Service, 2023. Soil Survey Geographic  
1223 Database (SSURGO). URL: <https://websoilsurvey.nrcs.usda.gov/>.  
1224 (Last Accessed: 2023-04-27).
- 1225 Naulin, J.P., Payrastre, O., Gaume, E., 2013. Spatially distributed flood  
1226 forecasting in flash flood prone areas: Application to road network super-  
1227 vision in Southern France. Journal of Hydrology 486, 88–99. Publisher:  
1228 Elsevier.
- 1229 Nielsen, E.R., Schumacher, R.S., 2020. Dynamical Mechanisms Supporting  
1230 Extreme Rainfall Accumulations in the Houston Tax Day 2016 Flood.  
1231 Monthly Weather Review 148, 83–109. doi:10.1175/MWR-D-19-0206.1.
- 1232 OpenStreetMap contributors, 2017. Planet dump retrieved from  
1233 <https://planet.osm.org>. <https://www.openstreetmap.org>.
- 1234 Panakkal, P., Juan, A., Garcia, M., Padgett, J.E., Bedient, P., 2019. To-  
1235 wards enhanced response: Integration of a flood alert system with road  
1236 infrastructure performance models, in: Structures Congress 2019: Build-  
1237 ings and Natural Disasters, American Society of Civil Engineers Reston,  
1238 VA. pp. 294–305.
- 1239 Panakkal, P., Price, A., Padgett, J., Bedient, P., 2022. Opensafe mo-  
1240 bility. <https://github.com/Pranavesh-Panakkal/OpenSafe-Mobility>.  
1241 (Last Accessed: 2022-10-04).
- 1242 Perica, S., Pavlovic, S., St. Laurent, M., Trypaluk, C., Unruh, D., Wilhite,  
1243 O., 2018. Precipitation-Frequency Atlas of the United States. Volume 11,  
1244 Version 2.0. Texas. doi:10.25923/1ceg-5094.

- 1245 Perks, M.T., Russell, A.J., Large, A.R., 2016. Advances in flash flood moni-  
1246 toring using unmanned aerial vehicles (UAVs). *Hydrology and Earth Sys-*  
1247 *tem Sciences* 20, 4005–4015. Publisher: Copernicus GmbH.
- 1248 Praharaj, S., Zahura, F.T., Chen, T.D., Shen, Y., Zeng, L., Goodall, J.L.,  
1249 2021. Assessing Trustworthiness of Crowdsourced Flood Incident Re-  
1250 ports Using Waze Data: A Norfolk, Virginia Case Study. *Transporta-*  
1251 *tion Research Record* 2675, 650–662. URL: <https://doi.org/10.1177/03611981211031212>, doi:10.1177/03611981211031212. publisher: SAGE  
1252 Publications Inc.
- 1253
- 1254 Pagnolato, M., Ford, A., Glenis, V., Wilkinson, S., Dawson, R., et al., 2017.  
1255 Impact of climate change on disruption to urban transport networks from  
1256 pluvial flooding. *Journal of Infrastructure Systems* 23, 04017015.
- 1257 Pyatkova, K., Chen, A.S., Butler, D., Vojinovi, Z., Djordjevi, S., 2019. As-  
1258 sessing the knock-on effects of flooding on road transportation. *Journal of*  
1259 *Environmental Management* 244, 48–60. doi:10.1016/j.jenvman.2019.  
1260 05.013.
- 1261 Rapidlasso GmbH, 2012. LAStools. URL: <https://rapidlasso.com/lastools/>. (Last Accessed: 2022-03-27).
- 1262
- 1263 Ravuri, S., Lenc, K., Willson, M., Kangin, D., Lam, R., Mirowski, P., Fitzsi-  
1264 mons, M., Athanassiadou, M., Kashem, S., Madge, S., et al., 2021. Skilful  
1265 precipitation nowcasting using deep generative models of radar. *Nature*  
1266 597, 672–677.

- 1267 Robinson, A.C., Chen, J., Lengerich, E.J., Meyer, H.G., MacEachren,  
1268 A.M., 2005. Combining Usability Techniques to Design Geovisualization  
1269 Tools for Epidemiology. *Cartography and geographic information science*  
1270 32, 243–255. URL: <https://www.ncbi.nlm.nih.gov/pmc/articles/PMC2786201/>, doi:10.1559/152304005775194700.
- 1272 Sebastian, A., Lendering, K., Kothuis, B., Brand, A., Jonkman, S., Gelder,  
1273 P., Kolen, B., Comes, T., Lhermitte, S., Meesters, K., Walle, B.,  
1274 Ebrahimi Fard, A., Cunningham, S., Khakzad, N., Nespeca, V., 2017.  
1275 Hurricane Harvey Report: A fact-finding effort in the direct aftermath of  
1276 Hurricane Harvey in the Greater Houston Region.
- 1277 Shand, T., Cox, R., Blacka, M., Smith, G., 2011. Australian rainfall and  
1278 runoff (ar&r). revision project 10: Appropriate safety criteria for vehicles;  
1279 report number: P10/s2/020. Water Research Laboratory, The University  
1280 of New South Wales: Manly Vale, Australia .
- 1281 Stern, R.E., Song, J., Work, D.B., 2017. Accelerated Monte Carlo system  
1282 reliability analysis through machine-learning-based surrogate models of  
1283 network connectivity. *Reliability Engineering & System Safety* 164, 1–9.  
1284 doi:10.1016/j.ress.2017.01.021.
- 1285 Sumalee, A., Ho, H.W., 2018. Smarter and more connected: Future intelli-  
1286 gent transportation system. *IATSS Research* 42, 67–71. doi:10.1016/j.  
1287 iatssr.2018.05.005.
- 1288 Texas Department of Transportation, 2022. Texas Department of Trans-

- 1289 portation - DriveTexas. URL: <https://drivetexas.org>. (Last Accessed:  
1290 2022-03-15).
- 1291 TranStar, H., 2022. Houston TranStar - Traffic Map. URL: [https://  
1292 traffic.houstontranstar.org/layers/](https://traffic.houstontranstar.org/layers/). (Last Accessed: 2022-03-27).
- 1293 Twitter, Inc., 2022. Twitter. URL: <https://twitter.com/home>. (Last Ac-  
1294 cessed: 2022-03-26).
- 1295 U.S. Census Bureau, 2022. 2022 tiger/line shapefiles: Census tracts.  
1296 URL: <https://www.census.gov/cgi-bin/geo/shapefiles/index.php>.  
1297 (Last Accessed: 2023-05-01).
- 1298 U.S. Department of Homeland Security, 2022. Homeland Infrastructure  
1299 Foundation-Level Data (HIFLD). URL: [https://hifld-geoplatform.  
opendata.arcgis.com/](https://hifld-geoplatform.<br/>1300 opendata.arcgis.com/). (Last Accessed: 2022-03-27).
- 1301 U.S. Geological Survey, 2022a. Flood Event Viewer - Hurricane Har-  
1302 vey. URL: <https://stn.wim.usgs.gov/fev/#HarveyAug2017>. (Last Ac-  
1303 cessed: 2022-03-27).
- 1304 U.S. Geological Survey, 2022b. USGS Water Data for the Nation. URL:  
1305 <https://waterdata.usgs.gov/nwis>. (Last Accessed: 2022-03-27).
- 1306 U.S. Geological Survey, 2023. The National Map. URL: [https://apps.  
nationalmap.gov/downloader/#/](https://apps.<br/>1307 nationalmap.gov/downloader/#/). (Last Accessed: 2023-04-27).
- 1308 Versini, P.A., Gaume, E., Andrieu, H., 2010. Application of a distributed hy-  
1309 drological model to the design of a road inundation warning system for flash

- 1310      flood prone areas. Natural Hazards and Earth System Sciences 10, 805–  
1311      817. doi:10.5194/nhess-10-805-2010. publisher: Copernicus GmbH.
- 1312      Vieux & Associates, Inc., 2022. About Gauge Adjusted  
1313      Radar Rainfall (GARR). URL: <https://www.vieuxinc.com/gauge-adjusted-radar-rainfall-garr/>. (Last Accessed: 2021-10-  
1314      20).  
1315
- 1316      Viikari, V.V., Varpula, T., Kantanen, M., 2009. Road-Condition Recognition  
1317      Using 24-GHz Automotive Radar. IEEE Transactions on Intelligent  
1318      Transportation Systems 10, 639–648. doi:10.1109/TITS.2009.2026307.
- 1319      Wickham, J., Stehman, S.V., Sorenson, D.G., Gass, L., Dewitz, J.A., 2021.  
1320      Thematic accuracy assessment of the NLCD 2016 land cover for the con-  
1321      terminous United States. Remote Sensing of Environment 257, 112357.  
1322      doi:10.1016/j.rse.2021.112357.
- 1323      Winsemius, H.C., Aerts, J.C.J.H., van Beek, L.P.H., Bierkens, M.F.P., Bouw-  
1324      man, A., Jongman, B., Kwadijk, J.C.J., Ligtvoet, W., Lucas, P.L., van  
1325      Vuuren, D.P., Ward, P.J., 2016. Global drivers of future river flood risk.  
1326      Nature Climate Change 6, 381–385. doi:10.1038/nclimate2893. number:  
1327      4 Publisher: Nature Publishing Group.
- 1328      Yin, J., Yu, D., Lin, N., Wilby, R.L., 2017. Evaluating the cascading impacts  
1329      of sea level rise and coastal flooding on emergency response spatial accessi-  
1330      bility in Lower Manhattan, New York City. Journal of Hydrology 555, 648–  
1331      658. URL: <https://www.sciencedirect.com/science/article/pii/S0022169417307321>, doi:10.1016/j.jhydrol.2017.10.067.

<sub>1333</sub> Zhang, W., Villarini, G., Vecchi, G.A., Smith, J.A., 2018. Urbanization exac-  
<sub>1334</sub> erbated the rainfall and flooding caused by hurricane Harvey in Houston.  
<sub>1335</sub> Nature 563, 384–388. doi:10.1038/s41586-018-0676-z. number: 7731  
<sub>1336</sub> Publisher: Nature Publishing Group.

<sub>1337</sub> Zhu, L., Yu, F.R., Wang, Y., Ning, B., Tang, T., 2019. Big Data Analytics  
<sub>1338</sub> in Intelligent Transportation Systems: A Survey. IEEE Transactions on  
<sub>1339</sub> Intelligent Transportation Systems 20, 383–398. doi:10.1109/TITS.2018.  
<sub>1340</sub> 2815678.